

# Quantum mechanical reactive scattering for three-dimensional atom plus diatom systems. II. Accurate cross sections for $H+H_2$ \*

George C. Schatz<sup>†</sup> and Aron Kuppermann

Arthur Amos Noyes Laboratory of Chemical Physics,<sup>‡</sup> California Institute of Technology, Pasadena, California 91125

(Received 22 December 1975)

Accurate three-dimensional reactive and nonreactive quantum mechanical cross sections for the  $H+H_2$  exchange reaction on the Porter-Karplus potential energy surface are presented. Tests of convergence in the calculations indicate an accuracy of better than 5% for most of the results in the energy range considered (0.3 to 0.7 eV total energy). The reactive differential cross sections are exclusively backward peaked, with peak widths increasing monotonically from about  $32^\circ$  at 0.4 eV to  $51^\circ$  at 0.7 eV. Nonreactive inelastic differential cross sections show backwards to sideways peaking, while elastic ones are strongly forward peaked with a nearly monotonic decrease with increasing scattering angle. Some oscillations due to interferences between the direct and exchange amplitudes are obtained in the para-para and ortho-to-ortho antisymmetrized cross sections above the effective threshold for reaction. Nonreactive collisions do not show a tendency to satisfy a " $j_z$ -conserving" selection rule. The reactive cross sections show significant rotational angular momentum polarization with the  $m_j = m'_j = 0$  transition dominating for low reagent rotational quantum number  $j$ . In contrast, the degeneracy averaged rotational distributions can be fitted to statistical temperaturelike expressions to a high degree of accuracy. The integral cross sections have an effective threshold total energy of about 0.55 eV, and differences between this quantity and the corresponding 1D and 2D results can largely be interpreted as resulting from bending motions in the transition state. In comparing these results with those of previous approximate dynamical calculations, we find best overall agreement between our reactive integral and differential cross sections and the quasiclassical ones of Karplus, Porter, and Sharma [J. Chem. Phys. **43**, 3259 (1965)], at energies above the quasiclassical effective thresholds. This results in the near equality of the quantum and quasiclassical thermal rate constants at 600 K. At lower temperatures, however, the effects of tunneling become very important with the quantum rate constant achieving a value larger than the quasiclassical one by a factor of 3.2 at 300 K and 18 at 200 K.

## I. INTRODUCTION

"The underlying physical laws necessary for the mathematical theory of a large part of physics and the whole of chemistry are thus completely known, and the difficulty is only that the exact application of these laws leads to equations much too complicated to be soluble." This legendary statement made by Dirac in 1929<sup>1a</sup> has been valid for the 50 years of existence of Schrödinger's wave mechanics,<sup>1b</sup> at least insofar as the dynamics of chemical reactions are concerned. Since the advent of electronic digital computers some 25 years ago, very large strides have been made in the accurate *ab initio* calculation of electronic wavefunctions of atoms and molecules, of electronic, vibrational, and rotational energy levels and of molecular equilibrium geometries. However, until very recently, the problem of accurately solving the Schrödinger equation describing the dynamics of even a very simple chemical reaction occurring on a given potential energy surface remained intractable, owing to both conceptual and computational difficulties. These difficulties have now been overcome, and the present paper describes accurate results obtained for the  $H+H_2$  hydrogen atom exchange reaction.

This simplest of chemical reactions has been of fundamental theoretical interest in the field of chemical dynamics ever since the beginning of quantum mechanics. Great progress in understanding it has been made both in the accurate determination of its ground state electronically adiabatic potential energy surface,<sup>2</sup>

and in the approximate calculation of the corresponding cross sections and other dynamical quantities.<sup>3-14</sup> A long sought objective of these dynamical studies has been the accurate quantum mechanical treatment of the three-dimensional collision dynamics. Such an accurate *ab initio* calculation for  $H+H_2$  is important, for this system has served as a prime example in the development and testing of approximate reaction dynamic theories such as quasiclassical methods,<sup>3,11c</sup> semiclassical methods,<sup>6,11d</sup> and approximate quantum methods.<sup>4,5,7,8,11,12</sup> In addition,  $H+H_2$  has been valuable in the development of transition state theory,<sup>15</sup> in the characterization of tunnelling<sup>14a,16</sup> and of the concept of vibrational adiabaticity,<sup>17</sup> and in analyzing the effects of changes in the potential energy surface on the reaction dynamics.<sup>18</sup> Much of our understanding of the influence of initial rotational<sup>9</sup> and vibrational<sup>14a</sup> state on chemical dynamics comes from studies on this system as does our knowledge concerning the influence of varying impact parameter<sup>3,11c</sup> or total angular momentum,<sup>5,7,11a,b</sup> of resonance and direct reaction mechanisms,<sup>3,19-21</sup> and other dynamical effects. Nonreactive elastic and inelastic  $H+H_2$  collisions have also been of theoretical interest in the analysis of rotational excitation and deactivation processes,<sup>11,13,22-25</sup> and in examining the nature of the competition and interference between reactive and nonreactive processes.<sup>11a,13b</sup> A number of reactive and nonreactive experimental studies of  $H+H_2$  and its isotopic counterparts have been done ranging from kinetic rate constant determinations<sup>26</sup> to hot atom<sup>27</sup> and molecular beam<sup>28</sup> experiments. The in-

teraction of theory and experiment has been of mutual benefit throughout their respective evolutionary developments.

In a previous paper<sup>29</sup> we presented a method for accurately solving the Schrödinger equation for the dynamics of the three-dimensional collision of an atom with a diatomic molecule on a single electronically adiabatic potential energy surface. This method was an extension of an earlier coplanar method<sup>30</sup> which has since been used extensively to study the  $2\text{DH} + \text{H}_2$  system.<sup>13</sup> In the present paper we describe the results of an application of this 3D procedure to  $\text{H} + \text{H}_2$ . These results include reactive and nonreactive transition probabilities, integral and differential cross sections, and reagent and product rotational state distributions. These results are extensively compared with those of earlier 3D approximate reactive and nonreactive calculations, and with 1D and 2D accurate ones. Some of the comparisons between the accurate 2D and 3D calculations were considered in preliminary communications,<sup>9,21</sup> and we shall elaborate upon them here by developing simple dynamical models for relating results of different dimensionality. Additional topics considered include the effects of indistinguishability of particles, angular momentum decoupling approximations, and thermal rate constants. In the present calculations, we use the semiempirical Porter-Karplus<sup>20</sup> potential surface. This surface has been the subject of several earlier studies, thus enabling comparisons of those results and ours without ambiguity being introduced by the use of different potentials. Results for the more accurate surface of Liu<sup>21</sup> (as parameterized by us) will be deferred to a later publication.

Section II provides a brief outline of the procedure used, and of the computational considerations governing convergence and accuracy. The results for the Porter-Karplus potential energy surface are given in Sec. III, and Sec. IV includes a summary of the more significant conclusions.

## II. THE CALCULATION

### A. Summarized description of the method

The method used to solve the Schrödinger equation for three-dimensional reactive and nonreactive  $\text{H} + \text{H}_2$  collisions has been extensively described in the preceding paper.<sup>29</sup> The space-fixed and body-fixed coordinates and systems of reference considered are described in Sec. II C and Fig. 2 of that paper. The calculation is done in body-fixed coordinates. Rotational motion is described by quantum numbers  $j_\lambda$  and  $\Omega_\lambda$ , where the tumbling quantum number  $\Omega_\lambda$  is associated with the tumbling angle  $\psi_\lambda$  and the component of rotational angular momentum along the  $Oz'_\lambda$  (body-fixed) axis which passes through atom  $A_\lambda$  and the center of mass of the  $A_\nu A_\kappa$  diatom. As shown previously,<sup>29</sup> the component of the orbital angular momentum about  $Oz'_\lambda$  is zero, so  $\Omega_\lambda$  is also associated with the projection of the total angular momentum along that axis. In order to simultaneously satisfy both criteria,  $\Omega_\lambda$  must obey the inequality

$$\Omega_\lambda \leq \min(J, j_\lambda), \quad (2.1)$$

where  $J$  is the total angular momentum quantum number.

Of crucial significance in the body-fixed coordinate system of Fig. 2 of the preceding paper is the fact<sup>29</sup> that the kinetic energy operator couples vibration-rotation states with different  $\Omega_\lambda$  tumbling quantum numbers but the same vibrational and rotational ones ( $v_\lambda j_\lambda$ ), while the potential energy coupling is diagonal in  $\Omega_\lambda$  but not in  $v_\lambda j_\lambda$ . This allows for the approximate separation of effects due to tumbling of the three atom plane about  $Oz'_\lambda$  from those due to the interaction potential energy, and we shall examine this separation in Sec. III. In addition, it provides for the natural development of centrifugal decoupling schemes, which will be discussed in future publication. Once the body-fixed fully coupled Schrödinger equations are set up, they are solved in two steps. The first one involves a numerical integration of these coupled equations through each arrangement channel region in coordinates appropriate to that region. This is followed by a second step in which the solutions thus generated in each of the three arrangement channel regions are smoothly matched to one another on a set of three surfaces which separate these regions in a symmetrized coordinate space in which all three arrangement channel coordinates are treated equivalently.<sup>31</sup> The resulting solutions, which are smooth and continuous everywhere, are then linearly combined to yield the appropriate reactance and scattering partial wave matrix solutions which are then combined to form the full scattering solutions. By using helicity representation scattering amplitudes, we obtain a very simple relationship between these amplitudes and the body-fixed partial wave scattering matrices  $\mathbf{S}_J$ , namely [from Eq. (5.31) of the preceding paper],

$$f_{\lambda\nu\lambda'j_\lambda m'_{j_\lambda}}^{\lambda'v'_\lambda j'_\lambda m'_{j'_\lambda}} = \left( \frac{\bar{V}_{v_\lambda j_\lambda}^\lambda}{\bar{V}_{v'_\lambda j'_\lambda}^{\lambda'}} \right)^{1/2} \frac{1}{2k_{v_\lambda j_\lambda}^\lambda} i^{j_\lambda - j'_\lambda + 1} \times \sum_{J=0}^{\infty} d_{m_{j_\lambda} m'_{j'_\lambda}}^J(\theta_{\lambda'}) (S_{\lambda\nu\lambda'j_\lambda m'_{j'_\lambda}}^{\lambda'v'_\lambda j'_\lambda m'_{j'_\lambda}} - S_{J\lambda\nu\lambda'j_\lambda m'_{j'_\lambda}}^{\lambda'v'_\lambda j'_\lambda m'_{j'_\lambda}}), \quad (2.2)$$

where the reagent state has  $m_{j_\lambda} = M = -\Omega_\lambda$  and the product state has  $m'_{j'_\lambda} = \Omega'_{\lambda'}$ , for all  $J$ .  $\bar{V}_{v_\lambda j_\lambda}^\lambda$  and  $k_{v_\lambda j_\lambda}^\lambda$  represent the appropriate (unscaled) velocities and wave numbers and

$$d_{m_{j_\lambda} m'_{j'_\lambda}}^J(\theta_{\lambda'})$$

is a Wigner rotation function (in the notation of Davydov)<sup>32</sup> of the scattering angle  $\theta_{\lambda'}$ .

For  $\text{H} + \text{H}_2$ , the problem can be simplified considerably because of arrangement channel symmetry and even-odd decoupling within each arrangement channel (as described in the preceding paper). A major consequence of these symmetry properties is that only two scattering amplitudes between a given initial state

$vjm_j$  and final state  $v'j'm'_j$  (where  $m'_j$  is an abbreviation for  $m'_j$ ) need be considered: the nonreactive (or direct) one (labeled  $N$ ) and the reactive (or exchange) one (labeled  $R$ ). Thus all the arrangement channel indices  $\lambda$  and  $\lambda'$  in Eq. (2.2) may be dropped as long as the symbols  $N$  or  $R$  are included as appropriate. As an additional consequence, nonreactive transitions between even and odd rotational states are forbidden. From the reactive and nonreactive scattering amplitudes  $f^N$  and  $f^R$ , one may then calculate differential (distinguishable atom) cross sections via

$$\sigma_{vjm_j \rightarrow v'j'm'_j}^{N,R}(\theta) = \frac{\bar{V}_{v'j'}}{\bar{V}_{vj}} |f_{vjm_j \rightarrow v'j'm'_j}^{N,R}|^2, \quad (2.3)$$

so that the integral cross section is given by

$$Q_{vjm_j \rightarrow v'j'm'_j}^{N,R} = \frac{\pi}{k_{vj}^2} \sum_{j=0}^{\infty} (2j+1) |T_{vjm_j \rightarrow v'j'm'_j}^{N,R}|^2, \quad (2.4)$$

where

$$T_{vjm_j \rightarrow v'j'm'_j}^N = \delta_{vjm_j \rightarrow v'j'm'_j} - S_{vjm_j \rightarrow v'j'm'_j}^N \quad (2.5a)$$

and

$$T_{vjm_j \rightarrow v'j'm'_j}^R = -S_{vjm_j \rightarrow v'j'm'_j}^R. \quad (2.5b)$$

$$\sigma_{vjm_j \rightarrow v'j'm'_j}^A = \frac{\bar{V}_{v'j'}}{\bar{V}_{vj}} \begin{cases} |f_{vjm_j \rightarrow v'j'm'_j}^N - f_{vjm_j \rightarrow v'j'm'_j}^R|^2 & (j, j' \text{ even, para} \rightarrow \text{para}) \\ 3 |f_{vjm_j \rightarrow v'j'm'_j}^R|^2 & (j \text{ even, } j' \text{ odd, para} \rightarrow \text{ortho}) \\ |f_{vjm_j \rightarrow v'j'm'_j}^R|^2 & (j \text{ odd, } j' \text{ even, ortho} \rightarrow \text{para}) \\ \{ |f_{vjm_j \rightarrow v'j'm'_j}^N + f_{vjm_j \rightarrow v'j'm'_j}^R|^2 + 2 |f_{vjm_j \rightarrow v'j'm'_j}^R|^2 \} & (j, j' \text{ odd, ortho} \rightarrow \text{ortho}). \end{cases} \quad (2.8)$$

For para-to-ortho (ortho-to-para) transitions, the antisymmetrized cross sections are proportional to the reactive ones, with a proportionality constant of 3 (1), so either quantity gives equivalent information. For other transitions, there will be interference between direct and exchange amplitudes as is implied in Eq. (2.8).

Since the rotational sublevels for a given vibration-rotation state are degenerate, we may define both integral and differential degeneracy-averaged cross sections by (valid for  $R$ ,  $N$ , or  $A$  transitions):

$$\sigma_{vj \rightarrow v'j'} = \frac{1}{2j+1} \sum_{m_j=-j}^j \sum_{m'_j=-j'}^{j'} \sigma_{vjm_j \rightarrow v'j'm'_j} \quad (2.9)$$

and

$$Q_{vj \rightarrow v'j'} = \frac{1}{2j+1} \sum_{m_j=-j}^j \sum_{m'_j=-j'}^{j'} Q_{vjm_j \rightarrow v'j'm'_j}. \quad (2.10)$$

We may also sum these cross sections over all final states, obtaining

$$\sigma_{vj}^N = \sum_{v'j'} \sigma_{vj \rightarrow v'j'}^N, \quad (2.11)$$

$$\sigma_{vj}^R = 2 \sum_{v'j'} \sigma_{vj \rightarrow v'j'}^R, \quad (2.12)$$

$$\sigma_{vj}^A = \sum_{v'j'} \sigma_{vj \rightarrow v'j'}^A, \quad (2.13)$$

The transition probability  $P_{vjm_j \rightarrow v'j'm'_j}^{N,R}$  is given by

$$P_{vjm_j \rightarrow v'j'm'_j}^{N,R} = |S_{vjm_j \rightarrow v'j'm'_j}^{N,R}|^2. \quad (2.6)$$

If we consider the effects of parity symmetry on the cross sections, we find<sup>33</sup>

$$\sigma_{vjm_j \rightarrow v'j'm'_j}^{N,R} = \sigma_{vjm_j \rightarrow v'j'-m'_j}^{N,R} \quad (2.7)$$

with analogous expressions valid for  $Q$  and  $P_j$ . The angle  $\theta$  of Eq. (2.3) refers to the direction of the scattered H atom with respect to the reagent H atom beam. For reactive collisions, a more customary angle to use is  $\theta_R$ , which is the angle of the product  $H_2$  with respect to the incident H, and is the supplement of  $\theta$  (i. e.,  $\theta_R = \pi - \theta$ ).

For  $H + H_2$ , the physically measurable cross sections must be obtained from wavefunctions which have been properly antisymmetrized with respect to interchange of any two nuclei. This can be done by the technique of postantisymmetrization as was detailed in the preceding paper, and leads to the following indistinguishable-atom differential cross sections (labeled by the symbol A):

with analogous expressions holding for the integral cross sections with  $Q$  substituted for  $\sigma$ . The factor of 2 in Eq. (2.12) arises from a sum over the two equivalent reactive arrangement channels (in a distinguishable-atom sense). Finally, we may wish to define the cross sections  $\sigma_{vj \rightarrow \text{para(ortho)}}^A$  in which the final state is restricted to being para (ortho). The corresponding expression is analogous to Eq. (2.13) with the sum over  $j'$  in the right-hand side restricted to even (odd) values, and a similar equation defines the integral cross section  $Q_{vj \rightarrow \text{para(ortho)}}^A$ .

## B. Convergence and accuracy tests and calculational details

In order to establish the reliability of the results of these calculations, a number of convergence and accuracy tests were performed, including (a) tests of flux conservation and microscopic reversibility, (b) tests of invariance of the results with respect to the inclusion of additional vibrational or rotational basis functions in the close coupling expansion, (c) tests of invariance of the results with respect to a change in the number of

TABLE I. Nonreactive (N) and reactive (R) transition probability matrices for  $E=0.60$  eV,  $J=0$ .<sup>a</sup>

$(v'j')$	$(vj)$						
	(00)	(01)	(02)	(03)	(04)	(05)	(06)
N							
(00)	0.0538	0	0.739	0	0.0195	0	0.398(-8)
(01)	0	0.460	0	0.226	0	0.215(-3)	0
(02)	0.741	0	0.0690	0	0.0303	0	0.761(-8)
(03)	0	0.226	0	0.742	0	0.219(-2)	0
(04)	0.0196	0	0.0304	0	0.948	0	0.822(-7)
(05)	0	0.222(-3)	0	0.219(-2)	0	0.998	0
(06)	0.328(-8)	0	0.642(-8)	0	0.867(-7)	0	1.000
R							
(00)	0.0249	0.0422	0.0219	0.425(-2)	0.251(-3)	0.249(-5)	0.334(-9)
(01)	0.0415	0.0713	0.0361	0.694(-2)	0.410(-3)	0.393(-5)	0.558(-9)
(02)	0.0220	0.0368	0.0183	0.331(-2)	0.177(-3)	0.172(-5)	0.279(-9)
(03)	0.421(-2)	0.699(-2)	0.327(-2)	0.537(-3)	0.273(-4)	0.338(-6)	0.544(-10)
(04)	0.257(-3)	0.411(-3)	0.183(-3)	0.280(-4)	0.177(-5)	0.462(-7)	0.431(-11)
(05)	0.280(-5)	0.451(-5)	0.202(-5)	0.406(-6)	0.601(-7)	0.215(-8)	0.116(-12)
(06)	0.197(-9)	0.318(-9)	0.147(-9)	0.285(-10)	0.337(-11)	0.113(-12)	0.767(-17)
Sums <sup>b</sup>	1.0005	1.0018	0.9981	0.9997	1.0000	1.0000	1.0000

<sup>a</sup>All projection quantum numbers  $m_j$  and  $m_j'$  are zero. Numbers in parentheses indicate the power 10 by which the number preceding it should be multiplied.

<sup>b</sup>Sum of probabilities from a given initial state over all possible final states and arrangement channels.

terms used to expand the potential [see Eq. (2.14) below], and (d) tests of invariance of the results with respect to a change in the nature of the reference potential  $V_{\text{ref}}(\gamma_\lambda, R_\lambda)$ <sup>29</sup> used to generate vibrational basis functions for the integration. Two additional tests are (e) the invariance of the results with respect to a change in the matching surface basis functions, and (f) the effects of lack of completeness of these matching surface functions on the ortho to para nonreactive transition probabilities. These latter two tests were not performed, but the analogous planar tests<sup>13b</sup> indicated that both effects were not important in that calculation. Since comparable planar and 3D vibration-rotation basis sets and matching surface functions were used in the two sets of calculations, we have assumed that the matching surface basis functions of Eq. (4.28) of the preceding paper will produce adequate (5% or better) convergence of the 3D results.

Conservation of flux and microscopic reversibility may be tested by examining the probability matrices for each partial wave, an example of which is given in Table I for total energy  $E=0.6$  eV and  $J=0$ . Flux conservation requires that the sum of each row or column of  $\mathbf{P}_j$  should equal unity, while microscopic reversibility requires that  $\mathbf{P}_j$  be symmetric. In the table we see that both of these properties are well satisfied (0.18% maximum deviation from flux conservation and 3% from symmetry for probabilities greater than  $10^{-4}$ ). In the results presented in this paper, we consider the energy range 0.3–0.7 eV. For energies  $E$  in the range 0.3–0.6 eV (including all  $J$ ), we find maximum deviations from flux conservation of 1% and from symmetry 10% (for nonnegligible probabilities). Between 0.6 and 0.7 eV we find 4% maximum deviations from flux conservation and 15% from symmetry. In order to obtain re-

sults of this quality, we used the vibration-rotation basis sets specified in Table II. For  $J=0$ , Eq. (2.1) greatly reduces the number of channels coupled, thus reducing computation time, allowing us to use more complete basis sets. This leads to excellent results for the  $J=0$  probabilities (with accuracies similar to or better than those in Table I at all energies considered). However, for larger  $J$ , the number of projections  $\Omega$  increases greatly. This leads to prohibitively large computation times if basis sets analogous to those for  $J=0$  are used. The ones actually used are those described in Table II. The above mentioned accuracy limits were obtained with them.

Convergence with respect to the inclusion of additional vibrational or rotational channels is examined in Table III. In Part A of that table, we examine several important transition probabilities at  $E=0.65$  eV,  $J=1$  for three different rotational basis sets (all with four vibrations). Upon changing from a  $j_{\text{max}}=5$  to a  $j_{\text{max}}=6$  basis set, we find changes of less than 1% in all probabilities. In Part B we examine several 0.65 eV,  $J=0$  probabilities with four and five vibrations (all with  $j_{\text{max}}=7$ ). Here we find 4% maximum change. An examination of the nature of the convergence properties with respect to the inclusion of additional basis functions was examined in greater detail in the planar calculation<sup>13b</sup> where we found that typically four vibrations and  $j_{\text{max}}=5$  were required for 5% convergence. A less extensive study of the three-dimensional results indicates similar convergence properties and the results of Table III are in agreement with this statement.

The two criteria (c) and (d) mentioned at the beginning of this section refer to changes in the representation of the potential  $V^\lambda(\gamma_\lambda, R_\lambda, \gamma_\lambda)$  [where  $\gamma_\lambda$  is the angle

TABLE II. Basis sets used and associated computation times for each partial wave.

$J$	No. of vibrations	$j_{\text{MAX}}^a$	Total No. of rotational states	$N^b$	Computation times (IBM 370/158) <sup>c</sup>		
					Number of channels	Integration time (min)	Total time (min)
0	4-6	7-11	8-12	32-60	40	11	14
1	4 or 5	5 or 6	14 or 18	56-90	90	42	54
2	4	5	22	88	88	37	48
3	4	4 or 5	20 or 26	92 <sup>d</sup>	92	36	47
$\geq 4$	4	4 or 5	20 or 30	100 <sup>e</sup>	100	47	61

<sup>a</sup> $j_{\text{MAX}}$  is the largest value of  $j$  within each rotational manifold.

<sup>b</sup>Total number of channels included in each arrangement channel.

<sup>c</sup>Computation times are for double precision arithmetic and the number of channels indicated and apply to computations for which both ortho-para and parity decoupling are used. The difference between the total time and the integration time is the time used in the matching procedure and asymptotic analysis.

<sup>d</sup>Refers to a basis with 26 rotational states for  $v=0, 1$ , and 20 for  $v=2, 3$ .

<sup>e</sup>Refers to a basis with 30 rotational states for  $v=0, 1$ , and 20 for  $v=2, 3$ .

between  $R_\lambda$  and  $r_\lambda$  (Fig. 1 of preceding paper)], and in the character of the reference potential  $V_{\text{ref}}^\lambda(r_\lambda, R_\lambda)$  used to generate the vibrational eigenfunctions. As detailed in the preceding paper, the potential is expanded in a series of Legendre polynomials

$$V^\lambda(r_\lambda, R_\lambda, \gamma_\lambda) = \sum_{k=0}^{\infty} V_k^\lambda(r_\lambda, R_\lambda) P_k(\cos \gamma_\lambda), \quad (2.14)$$

where, for an atom plus homonuclear diatomic molecule system like  $\text{H} + \text{H}_2$ , the sum over  $k$  includes only even terms. In an actual calculation, Eq. (2.14) is truncated after  $n$  terms (such as  $n=3$ ). This procedure is justified if the resulting probabilities are not significantly changed when an additional term is added. To evaluate the effects of changing  $n$ , we compare in Table IV the results of calculations with  $n=2, 3, 4$ , and  $5^{34}$  for selected transition probabilities at two different energies. Although the  $n=2$  results are often significantly in error (by as much as 30%), we find less than 7% changes in going from  $n=3$  to  $n=4$  and virtually no change at all in going from  $n=4$  to  $n=5$ . All calculations of this paper other than those whose results are presented in Table IV used  $n=3$ . The reference potential  $V_{\text{ref}}^\lambda$  which is used to numerically generate the vibrational basis functions according to the procedure of Ref. 29 still allows for some freedom of choice in the interaction region due to nonseparability of vibrational motions from translational or rotational ones. In the coplanar calculations, two different choices of the reference potential [ $V_{\text{ref}}^\lambda = V(r_\lambda, R_\lambda, \gamma_\lambda=0)$  and  $V_{\text{ref}}^\lambda = V_0^\lambda(r_\lambda, R_\lambda)$ ] were used. A comparison of these calculations indicated that for basis sets with four or more vibrations, the results from the two reference potentials differed by less than 5%. A limited number of three-dimensional calculations indicates a behavior comparable to the planar case.

### III. RESULTS FOR THREE-DIMENSIONAL $\text{H} + \text{H}_2$

#### A. Transition probabilities

In this section we examine the  $J$  dependence of the reactive and inelastic transition probabilities in the energy range 0.3-0.7 eV. Figures 1(a) and 2(a) present the

reactive probabilities  $P_{J,00-01}^R$  (summed over final  $m_j'$ ). These figures indicate that the probability is a rapidly decreasing function of  $J$  with a peak near  $J=0$  for all but the highest energy considered. If we define  $J_{\text{MAX}}$  as the lowest value of  $J$  for which  $P_{J,vj-v'j'}^R$  has decreased to less than 1% of its maximum value, then  $J_{\text{MAX}}$  is 4 at 0.3 eV and increases monotonically to about 10 at 0.7 eV. The contributions of these transition probabilities to the integral reaction cross sections are weighted by the factor  $2J+1$  [see Eqs. (2.4)-(2.6)]. Figures 1(b) and 2(b) depict the product  $(2J+1)$

TABLE III. Nonreactive and reactive transition probabilities for  $E=0.65$  eV.

Transition ( $vj \rightarrow v'j'$ )	Reactive or nonreactive	Basis set		
		$a(N=56)$	$b(N=72)$	$c(N=64)$
A. $J=1, m_j=m_j'=0$				
00-02	N	0.531	0.527	0.531
01-03	N	0.193	0.186	0.186
00-00	R	0.0404	0.0408	0.0402
00-01	R	0.0740	0.0741	0.0739
01-01	R	0.134	0.135	0.134
		$d(N=32)$	$e(N=40)$	
B. $J=0, m_j=m_j'=0$				
00-02	N	0.517	0.512	
01-03	N	0.223	0.216	
00-00	R	0.0432	0.0434	
00-01	R	0.0780	0.0802	
01-01	R	0.145	0.150	
Basis sets <sup>a</sup>				
a. 4 vibrations, 14 rotations/vibration ( $j_{\text{MAX}}=5$ )				
b. 4 vibrations, 18 rotations/vibration ( $j_{\text{MAX}}=6$ )				
c. 4 vibrations, 18 rotations for $v=0, 1$ ; 14 for $v=3, 4$				
d. 4 vibrations, 8 rotations/vibration ( $j_{\text{MAX}}=7$ )				
e. 5 vibrations, 8 rotations/vibration ( $j_{\text{MAX}}=7$ )				

<sup>a</sup>In each basis set, all values of the projection quantum numbers compatible with angular momentum restrictions and with matching restrictions were included (see Sec. II A and preceding paper).

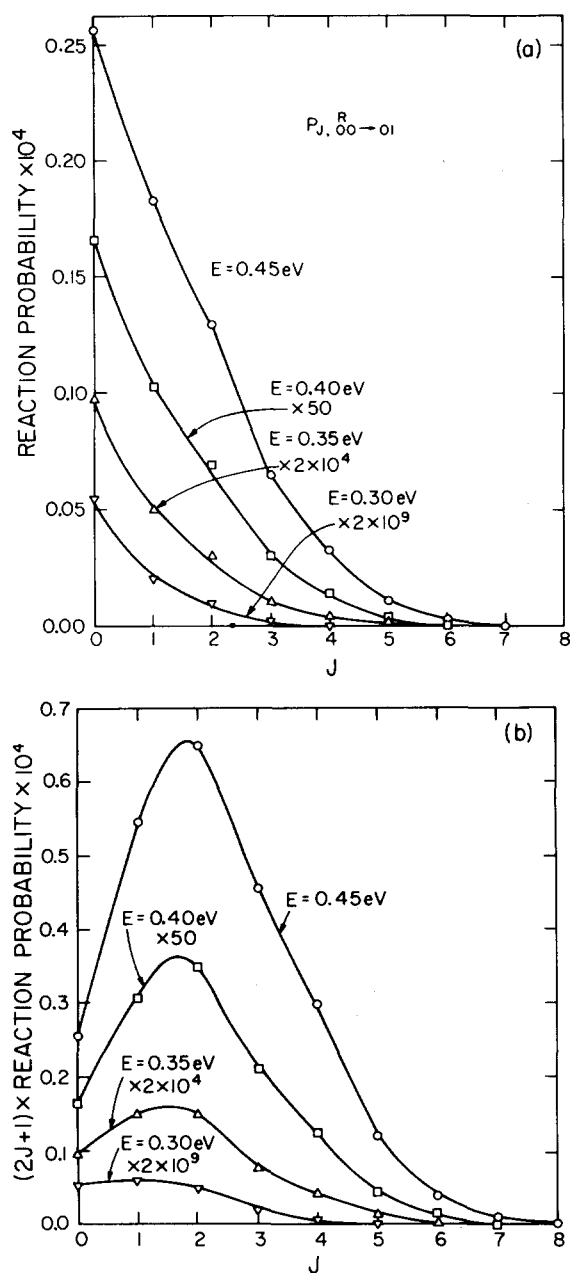


FIG. 1. (a) Reaction probability  $P_{J,00-01}^R$  (summed over final  $m_j$ ) as a function of  $J$  for total energies  $E = 0.30, 0.35, 0.40$ , and  $0.45$  eV. (b) The same reaction probabilities multiplied by  $2J+1$ . The scale factors indicated for the last three energies are the numbers by which the probabilities were multiplied before being plotted.

$\times P_{J,00-01}^R$ , and we see that the partial wave which gives the largest contribution to  $Q_{00-01}^R$  varies from  $J=1$  at  $0.3$  eV to  $J=4$  at  $0.7$  eV. To examine the contributions of the different projection quantum numbers to the curves in Figs. 1(a) and 2(a), we plot in Fig. 3 the reaction probabilities  $P_{J,00-01m_j}^R$  for  $m_j = 0, \pm 1$  (and their sum) at  $E = 0.6$  eV. It is apparent from the figure that  $m_j = 0$  makes the dominant contribution to  $P_{J,00-01}^R$  for this transition at all  $J$  for which the transition probability is nonnegligible. The  $m_j = \pm 1$  probability [which, from the  $P_J$  analog of Eq. (2.7), is independent of the sign of  $m_j$ ] shows a peak near  $J=4$  followed by a somewhat slower de-

crease with increasing  $J$  than is exhibited by the  $m_j = 0$  probability. An examination of other transition probabilities at  $0.6$  eV indicates that in general, the  $m_j = 0$  to  $m_j' = 0$  reaction probability is the dominant one for a given  $v_j$  and  $v_j'$ . This effect becomes less important as either  $J$ ,  $j$ , or  $j'$  increase, as is illustrated in Fig. 4 for the probability  $P_{J,00-03m_j}^R$ , but it remains a general fact that the  $m_j = m_j' = 0$  transition probability is the largest one for  $J < J_{MAX}$  and  $j \leq 4$ . This statement is also true for other energies considered. Its effect on the integral cross sections will be discussed in Sec. III C.

Let us now consider the meaning of this rotational

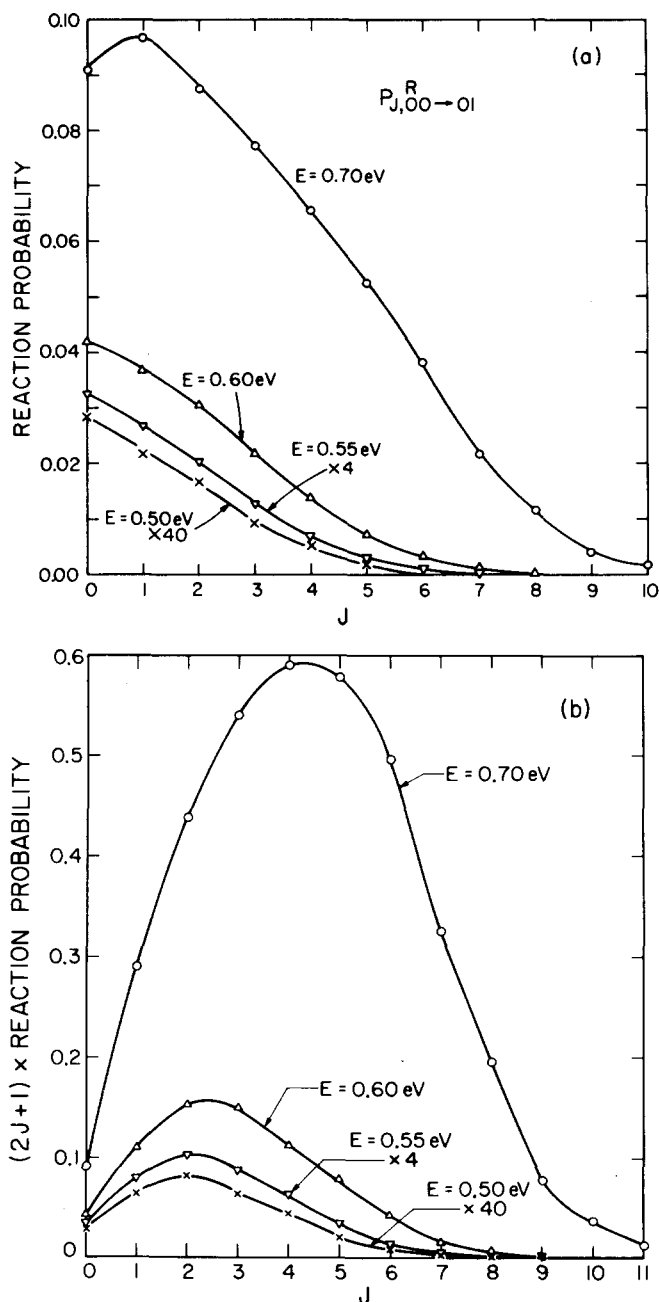


FIG. 2. (a) Reaction probability  $P_{J,00-01}^R$  analogous to Fig. 1 as a function of  $J$  at  $E = 0.50, 0.55, 0.60, 0.65$ , and  $0.70$  eV. (b)  $2J+1$  times these reaction probabilities. Scale factors have the same meaning as in Fig. 1.

TABLE IV. Convergence of selected<sup>a</sup> nonreactive and reactive transition probabilities with respect to number of terms included in expansion of  $V(\gamma_\lambda, R_\lambda, \gamma_\lambda)$ .<sup>b</sup>

Energy	$(vj) \rightarrow (v'j')$	Reactive or nonreactive	Number of terms			
			2	3	4	5
0.55 eV	00 → 02	N	0.737	0.707	0.706	0.706
	01 → 03	N	0.153	0.161	0.161	0.161
	00 → 00	R	0.720(-2)	0.483(-2)	0.511(-2)	0.514(-2)
	00 → 01	R	0.0119	0.811(-2)	0.838(-2)	0.847(-2)
	01 → 01	R	0.0206	0.0130	0.0135	0.0135
0.625 eV	00 → 02	N	0.605	0.642	0.629	0.624
	01 → 02	N	0.206	0.225	0.224	0.220
	00 → 00	R	0.0400	0.0353	0.0372	0.0377
	00 → 01	R	0.0726	0.0641	0.0655	0.0673
	01 → 01	R	0.128	0.115	0.117	0.120

<sup>a</sup>Only  $J=m_j=m'_j=0$  transition probabilities are considered in this comparison. Notation is analogous to Table I. Numbers in parentheses indicate the power of 10 by which the numbers preceding them should be multiplied.

<sup>b</sup>The expansion is given in Eq. (2.14).

projection quantum number "quasi selection rule." In the helicity representation being used, the rotational wavefunction of the diatom at large distances from the atom is  $Y_{j\lambda m_\lambda}(\gamma_\lambda, \psi_\lambda)$  before the collision (except for a phase factor) and

$$Y_{j\lambda' m'_\lambda}(\gamma_{\lambda'}, \psi_{\lambda'})$$

after the collision. For the Porter-Karplus potential used,<sup>2c</sup> linear orientations, corresponding to  $\gamma_\lambda$  and  $\gamma_{\lambda'}$  equal to 0 or  $\pi$ , greatly favor reaction over other orientations. (The linear barrier height is 0.396 eV, while the perpendicular one is about 2.8 eV.) Since those spherical harmonics have nodal lines along these directions unless the polar component of the angular momentum vanishes, we conclude that the  $m_j=m'_j=0$  reaction probabilities should be larger than all others, in agreement with our results. This can be visualized classically

by recalling that initially  $\Omega = -m_j$ , so that  $m_j=0$  implies (for nonzero  $j$ ) that the axis of rotation is perpendicular to the direction of approach, as schematically indicated in Fig. 5. In this situation, twice during each diatom rotation the three atoms go through a collinear configuration (for zero impact parameter collisions). For  $m_j \neq 0$  no collinear configurations are sampled. After the collision,  $m'_j = \Omega'$  so that again only for  $m'_j=0$  can we have a postcollision linear orientation (regardless of the scattering angle). We should also note that the isolated diatom rotational period  $\{2.7 \times 10^{-13} / [j(j+1)]^{1/2} \text{ sec}\}^3$  is generally larger than the interaction time (which is less than  $3 \times 10^{-14} \text{ sec}$ <sup>35</sup> for the energies considered here) so that the rotational motions are generally slow compared to collision times at these energies and the collision orientation does not change rapidly during the approach and departure steps. This

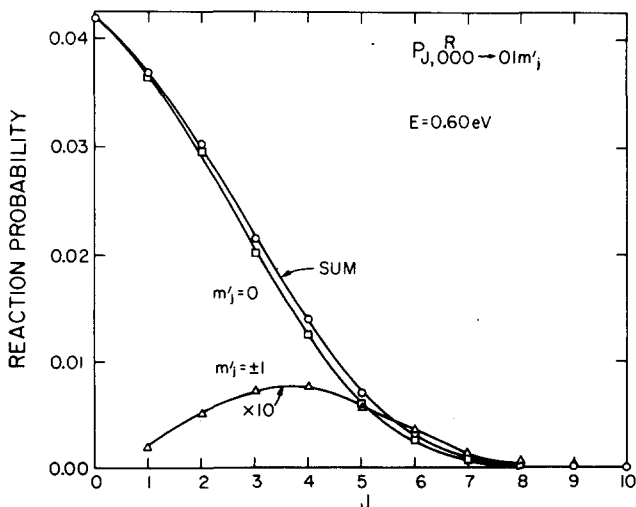


FIG. 3. Reaction probability  $P_{J,000-01m'_j}^R$  vs  $J$  for  $m'_j=0, \pm 1$  at 0.60 eV total energy ( $E_0=0.328$  eV). Curve labeled sum is the sum of the probabilities over  $m'_j$ . Scale factor has the same meaning as in Fig. 1.

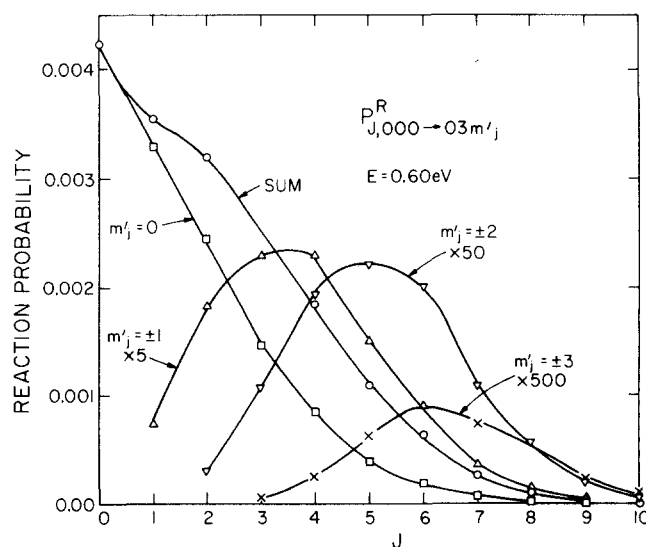


FIG. 4. Reaction probability  $P_{J,000-03m'_j}^R$  vs  $J$  for  $m'_j=0, \pm 1, \pm 2, \pm 3$  at 0.60 eV total energy, analogous to Fig. 3.

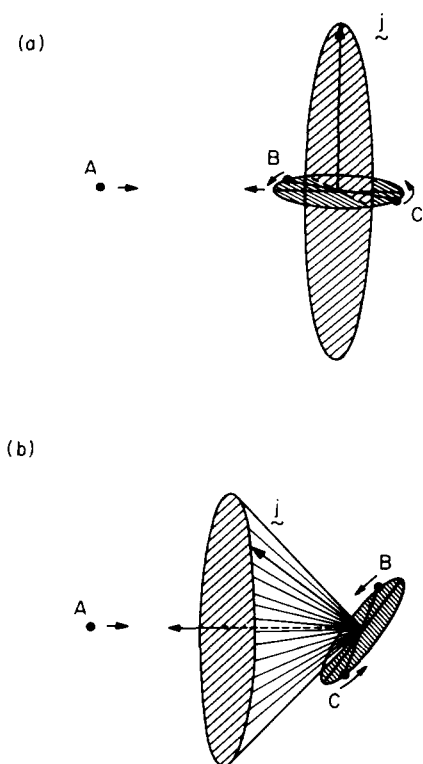


FIG. 5. Influence of projection quantum number  $m_j$  (for  $j > 0$ ) on the allowed relative orientations of atom (A) with respect to diatom (BC) for zero impact parameter collisions: (a)  $m_j = 0$  initially so that the rotational angular momentum vector is perpendicular to direction of relative motion; (b)  $m_j > 0$  initially so that the  $j$  vector lies on a cone about the relative motion vector and makes an acute angle with it. In both (a) and (b) the rotation plane of the diatom is indicated by the smaller ellipse.

analysis indicates not only that the  $m_j = m'_j = 0$  reaction probability should be larger than all others, as pointed out above, but also explains why this rule becomes less rigid for large  $J$  (in which case nonzero impact parameter collisions can lead to linear orientations for  $m_j, m'_j \neq 0$ ) and for large  $j$  (where the diatom rotates fast enough to change the orientation rapidly during the collision, thus reducing the advantage of a linear orientation at any one point during the collision). As a second prediction of this model, we would expect that those transition probabilities for which  $m_j = 0$  or  $m'_j = 0$  (but not both) and the corresponding integral reaction cross sections should dominate over those for which neither  $m_j$  nor  $m'_j$  are zero. We shall see in Sec. III C that this prediction is correct. We emphasize that this projection quantum number selection rule presupposes (a) a potential surface which favors linear orientations, and (b) that the projection quantum numbers are referenced to the body fixed coordinate system of Fig. 2 of the preceding paper. The latter condition is important because it singles out the  $m_j$  or  $m'_j = 0$  collisions as leading to a linear collision orientation with a greater probability than  $m_j$  or  $m'_j \neq 0$ . By rotating the quantization axis to another direction (such as one perpendicular to the three-atom plane as is done for the coplanar reaction, or along a space-fixed direction), the body-fixed projections would become mixed and we would not be able to unscramble the information as easily.

Figure 6 shows the  $J$  dependence of the phases of the scattering matrix elements  $S_{J,000 \rightarrow 01m'_j}^R$  for  $m'_j = 0, \pm 1$  at 0.6 eV (the same transitions considered in Fig. 3). It is important to note that the phase is most slowly varying near  $J=0$ . Semiclassically this implies that the deflection angle should be small for small impact parameter collisions.<sup>36</sup> This implies that a small scattering angle  $\theta$  will result from these low  $J$  collisions, or, equivalently, a reactive scattering angle  $\theta_R$  near  $180^\circ$ .

In Fig. 7(a) we examine the nonreactive transition probability  $P_{J,000 \rightarrow 02m'_j}$ , and its sum over final  $m'_j$  at 0.6 eV as a function of  $J$ . Here we find  $J_{\text{MAX}} = 30$ , so that a much larger number of partial waves contribute to the nonreactive cross section than is the case for the reactive transitions in Figs. 1-4. Note that the  $m'_j = 0$  transition probability is dominant only for very small  $J (< 3)$  indicating that the linear orientation rule is probably not significant here (as might be expected for a nonreactive collision where the nature of the potential in the transition state is of lesser significance than it is for reactive collisions). An examination of other nonreactive transition probabilities indicates no strong tendency for a  $m_j = -m'_j$  ( $\Omega = \Omega'$ ) " $j_z$ -conserving" selection rule as has been assumed in rotationally inelastic scattering,<sup>37</sup> thus indicating that the strong coupling or sudden limit does not apply to H + H<sub>2</sub> inelastic collisions for the potential used. We shall examine this again in a separate publication. The transition probabilities of Fig. 7(a) may also be expressed in terms of the orbital angular momentum quantum number  $l$  (as might be used in a space-fixed analysis) by performing a unitary transformation on the body-fixed scattering matrix [see Eqs. (5.14) and (5.15) of Ref. 29]. Figure 7(b) indicates the resulting transition probabilities for  $E = 0.60$  eV (the sum over projections

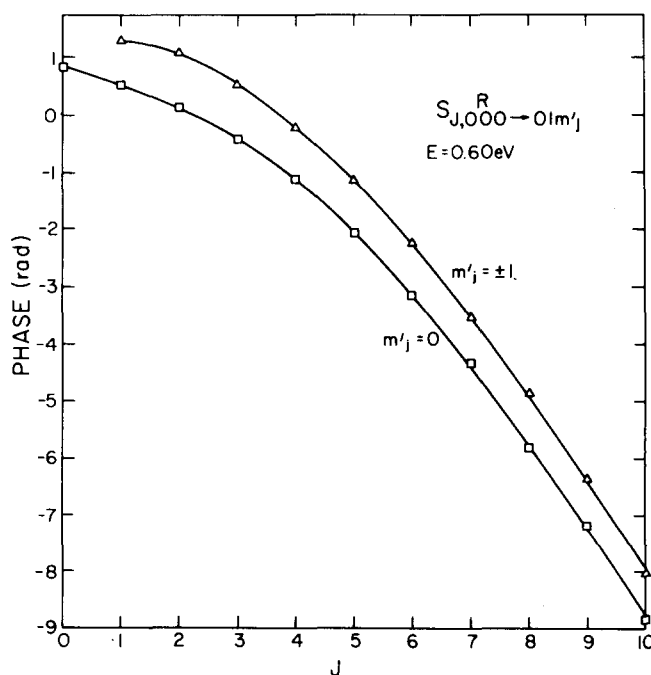


FIG. 6. Phases of  $S_{J,000 \rightarrow 01m'_j}^R$  for  $m'_j = 0, \pm 1$  as a function of  $J$  at  $E = 0.60$  eV.

being an invariant). Here we again see no particular selection rule governing the transition probabilities.

### B. Differential cross sections

In Figs. 8 and 9 we plot the antisymmetrized para-to-ortho differential cross sections  $\sigma_{00 \rightarrow 01}^A$  as a function of the reactive scattering angle  $\theta_R$ . From Eqs. (2.3) and (2.8) it should be apparent that these cross sections are just 3 times the distinguishable atom  $\sigma_{00 \rightarrow 01}^R$ . We see in both figures that the reactive cross section is strongly backward peaked at all energies considered in the calculation. The width of the backward peak at half-maximum is  $48^\circ$ ,  $32^\circ$ ,  $33^\circ$ ,  $41^\circ$ , and  $51^\circ$  at  $E=0.3$ , 0.4, 0.5, 0.6, and 0.7 eV, respectively. At the threshold energy of the process considered, one would normally expect isotropic scattering since only the  $J=0$  partial wave would contribute to the cross section. At 0.3 eV, Fig. 1 indicates that partial waves other than  $J=0$  still contribute significantly ( $J_{MAX}=4$ ), so that the differential cross section is backward peaked, but rather broad. The width of this peak decreases with increasing energy above 0.3 eV to a minimum near 0.4 eV. As  $E$  increases further, the width begins to increase, presumably as a result of increased contributions of larger impact parameter collisions (from Figs. 1, 2) to the reaction cross section.

As was the case in the coplanar reaction,<sup>13b</sup> the shape of the differential cross section is a sensitive test of the accuracy of the calculation. Small inaccuracies in

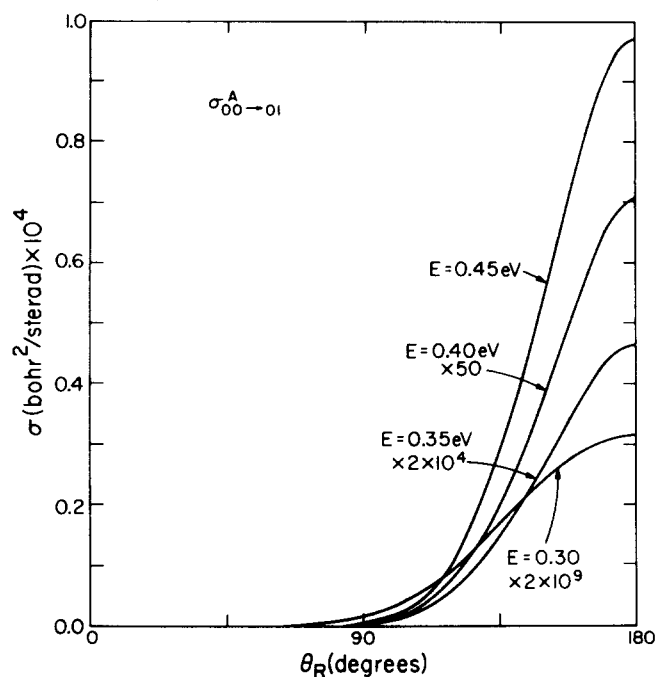


FIG. 8. Differential cross sections  $\sigma_{00 \rightarrow 01}^A$  as a function of the reactive scattering angle  $\theta_R = 180^\circ - \theta$  at the same energies as were considered in Fig. 1. Scale factors have the same meaning as in that figure.

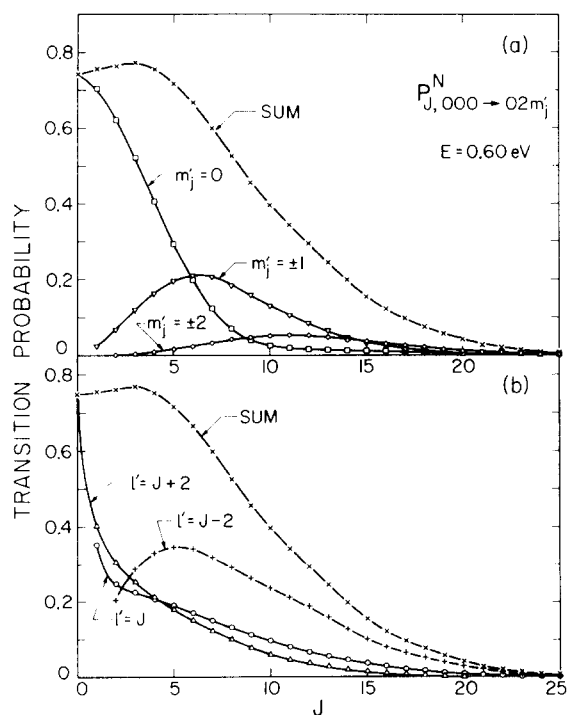


FIG. 7. (a) Nonreactive body-fixed transition probability  $P_{J, 000 \rightarrow 02m_j}^N$  as a function of  $J$  at 0.60 eV total energy for  $m_j = 0, \pm 1, \pm 2$ . Curve labeled sum is the sum of these five probabilities. (b) Analogous space-fixed probabilities for the three orbital angular momenta  $l' = J, J+2, J-2$ . The sum is invariant to the use of body-fixed or space-fixed representations.

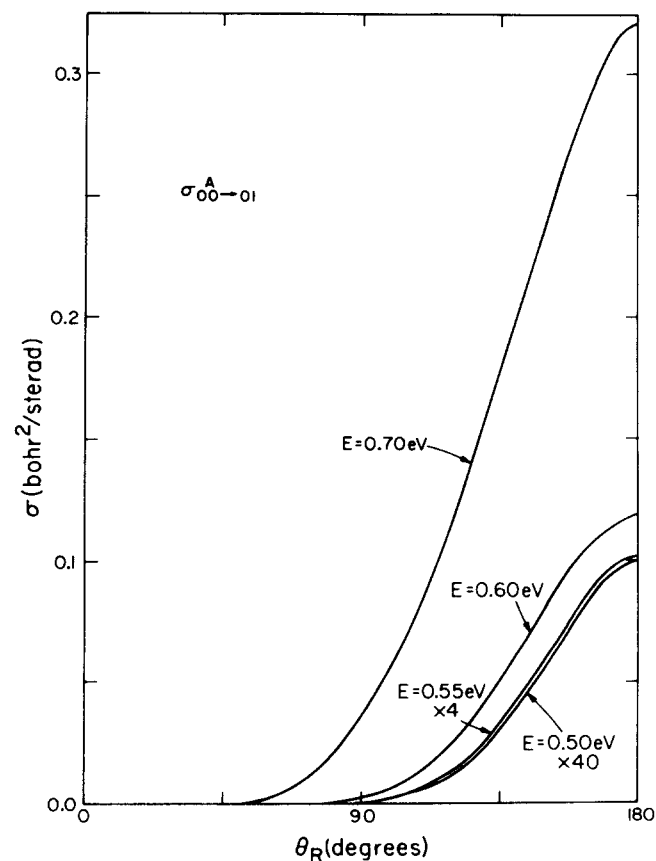


FIG. 9. Differential cross sections  $\sigma_{00 \rightarrow 01}^A$ , as in Fig. 8 for the same energies considered in Fig. 2. Scale factors have the same meaning as in Fig. 1.

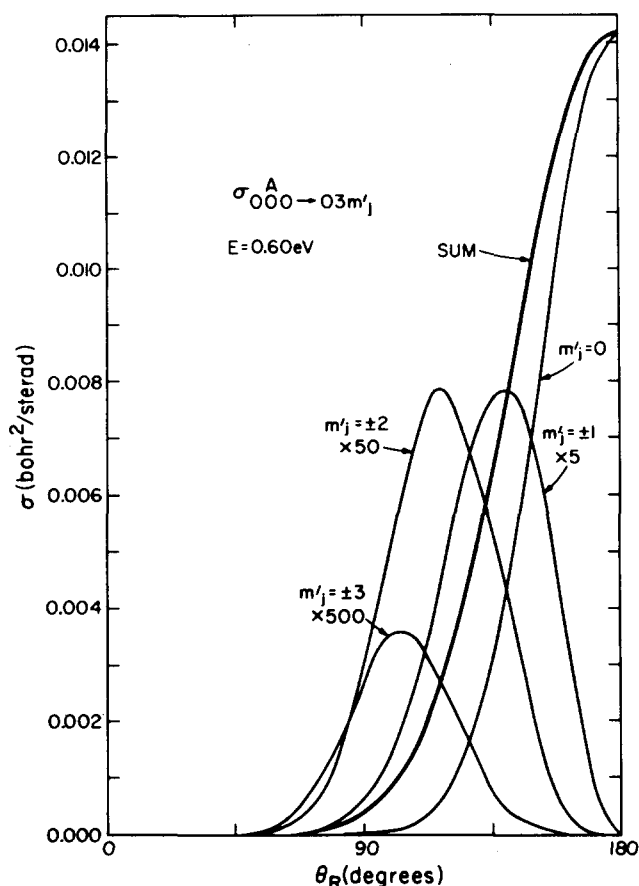


FIG. 10. Differential cross section  $\sigma_{000-03m'_j}^A$  as a function of reactive scattering angle  $\theta_R = 180^\circ - \theta$  for  $m'_j = 0, \pm 1, \pm 2, \pm 3$  at  $E = 0.60$  eV. Curve labeled sum is the sum of all seven cross sections and is equal to the degeneracy-averaged  $\sigma_{000-03}^A$ . Scale factors have the same meaning as in Fig. 1.

either the magnitudes or phases of the scattering matrix elements for any partial wave can result in spurious oscillations in the differential cross sections. In addition, premature truncation of the partial wave sum [Eq. (2.2)] can lead to a spurious forward peaking. In order to avoid such spurious oscillations in the cross sections, we checked convergence at several values of  $J$  (by the criteria of Sec. II B) and found that equivalent convergence had been attained at all  $J$ . [Recall from Table II that the nature of the vibration-rotation basis set has to be changed for each  $J$  ( $J \leq 4$ ).] Premature truncation of the partial wave sum was avoided by requiring that the reactive probabilities at the cutoff value  $J_c$  be no larger than  $10^{-4}$  times those at  $J = 0$ . In general, we found  $J_c \sim J_{MAX} + 5$ . Both Figs. 8 and 9 show essentially no indication of spurious oscillations or forward peaking (typically the  $\theta_R = 0$  cross section is 200 to 1000 times smaller than the  $\theta = 180^\circ$  result). We should also note that the appearance of Figs. 8 and 9 is quite typical of all degeneracy-averaged para-to-ortho and ortho-to-para cross sections.

To examine the  $m_j$  dependence of the differential cross sections, we plot in Fig. 10  $\sigma_{000-03m'_j}^A$  for  $m'_j = 0, \pm 1, \pm 2, \pm 3$ , and their sum. (The corresponding probabilities were considered in Fig. 4.) We see that only the  $m'_j = 0$  projection gives scattering peaked in the back-

ward  $\theta_R = 180^\circ$  direction. As  $|m'_j|$  increases from zero, we find a shift towards more forward scattering with the cross sections peaking at  $\theta_R = 139^\circ, 117^\circ$ , and  $102^\circ$  for  $|m'_j| = 1, 2, 3$ , respectively. Much of the structure of the angular distributions in Fig. 10 can be understood by examining Eq. (2.2). The Wigner rotation function<sup>32</sup>  $d_{0m'_j}^J(\theta)$  is proportional to the associated Legendre function  $P_{m'_j}^J(\cos\theta)$  and is therefore proportional to  $(\sin\theta)^{|m'_j|}$  times a polynomial in  $\cos\theta$ . Since  $\theta_R = \pi - \theta$ , the  $\sigma_{000-03m'_j}^A$  should have a  $(\sin\theta_R)^{2|m'_j|}$  envelope and, for  $m'_j \neq 0$ , vanish at  $\theta_R = 0$  and  $180^\circ$ . Indeed, one can qualitatively obtain the  $m'_j = \pm 1$  curve by multiplying the  $m'_j = 0$  one by  $\sin^2\theta_R$  and similar prescriptions can be used for the higher  $m'_j$  curves. The vanishing of the  $m'_j \neq 0$  cross sections at  $\theta_R = 0^\circ$  and  $180^\circ$  is also a consequence of angular momentum conservation. To see this, we recall that the incident plane wave solution is an eigenfunction of  $J_z$ , the operator corresponding to the projection of the total angular momentum along the space-fixed  $z$  axis, with eigenvalue  $M = m_j$  (since  $m_l$ , the  $z$  component of the orbital angular momentum, is initially zero for the plane wave solution). Since  $J_z$  commutes with the Hamiltonian,<sup>38</sup>  $M$  will be a good quantum number, i. e.,  $J_z \Psi^{M\lambda}[P] = M\hbar \Psi^{M\lambda}$  everywhere in configuration space. In particular, for  $\theta_R = 0^\circ$  ( $180^\circ$ ), the final  $Oz'_\lambda$  axis<sup>39</sup> will be antiparallel (parallel) to the initial  $Oz$  axis, so that conservation of  $J_z$  requires that the outgoing projection quantum number  $m'_j$  must equal  $-M$  ( $+M$ ), unless the corresponding scattering amplitude vanishes in that direction. Therefore, if the corresponding scattering amplitudes do not vanish, we must have  $m_j = M = -m'_j$  for  $\theta_R = 0^\circ$  and  $m_j = M = m'_j$  for  $\theta_R = 180^\circ$ . Applying this reasoning to the  $\sigma_{000-03m'_j}^A$  cross section, we conclude that for  $m'_j \neq 0$ ,  $J_z$  cannot be conserved for  $\theta_R = 0^\circ$  or  $\theta_R = 180^\circ$  unless that cross section vanishes in both of those directions, in agreement with the conclusion reached above. Finally we should point out that the dominance of the  $m'_j = 0$  component of  $\sigma_{000-03m'_j}^A$  in Fig. 10 is again a consequence of the favored linear transition state geometry, discussed in Sec. III A. The  $m'_j = 0$  collisions for small impact parameters have a significant reaction probability only for linear or nearly linear configurations which leads to the observed dominant backward scattering for this transition. For  $m'_j \neq 0$ , the collision configurations are nonlinear (at least in the product arrangement channel) and we would expect to see the sideways scattering exhibited in Fig. 10.

In Fig. 11 we plot the nonreactive differential cross sections  $\sigma_{000-02m'_j}^N$  ( $m'_j = 0, \pm 2$ , and summed) at  $E = 0.6$  eV as a function of  $\theta$ . Here the predominant scattering direction is approximately  $90^\circ$  although significant cross sections are obtained at all angles. The structure in these curves in the forward direction ( $\theta < 15^\circ$ ) may be a spurious artifact introduced by small errors in the phases of certain large  $J$  elements of  $\mathbf{S}_J$  (see related discussion of Ref. 22). Our previous analysis regarding the individual  $m'_j$  cross sections in the  $\theta = 0^\circ$  and  $180^\circ$  directions applies to Fig. 11 as well. We note, however, that the absence of a linear or near linear orientation restriction in nonreactive collisions leads to significant cross sections at all  $m'_j$  and at all

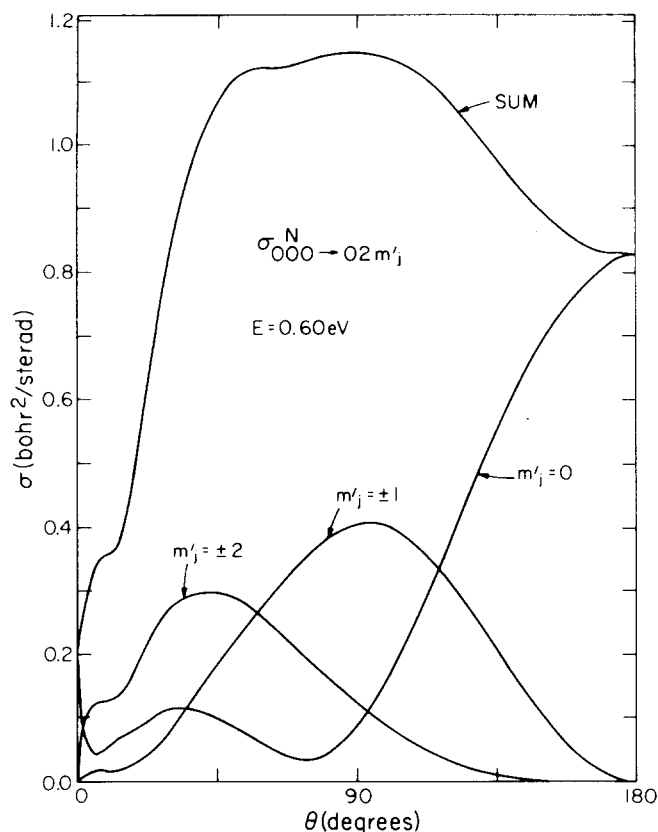


FIG. 11. Differential nonreactive cross section  $\sigma_{000 \rightarrow 02 m'_j}^N$  as a function of scattering angle  $\theta$  for  $m'_j = 0, \pm 1, \pm 2$  at  $E = 0.60$  eV. Curve labeled sum is the sum of all five cross sections and is equal to the degeneracy-averaged  $\sigma_{00 \rightarrow 02}^N$ .

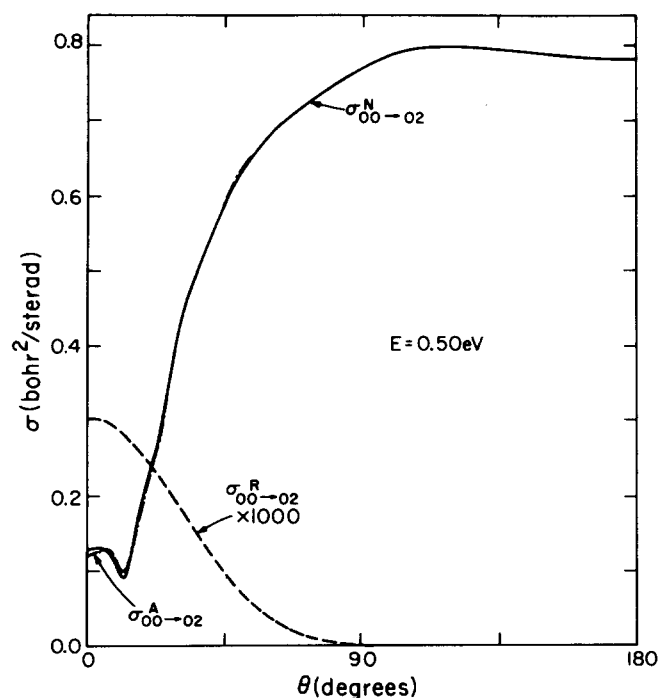


FIG. 12. Degeneracy-averaged differential cross sections  $\sigma_{00 \rightarrow 02}^N$ ,  $\sigma_{00 \rightarrow 02}^R$ , and  $\sigma_{00 \rightarrow 02}^A$  as a function of scattering angle  $\theta$  at  $E = 0.50$  eV ( $E_0 = 0.228$  eV). The nonreactive and antisymmetrized curves are essentially identical for  $\theta > 20^\circ$ . Note the use of  $\theta$  rather than  $\theta_R$  for plotting the reactive differential cross section. The scale factor has the same meaning as in Fig. 1.

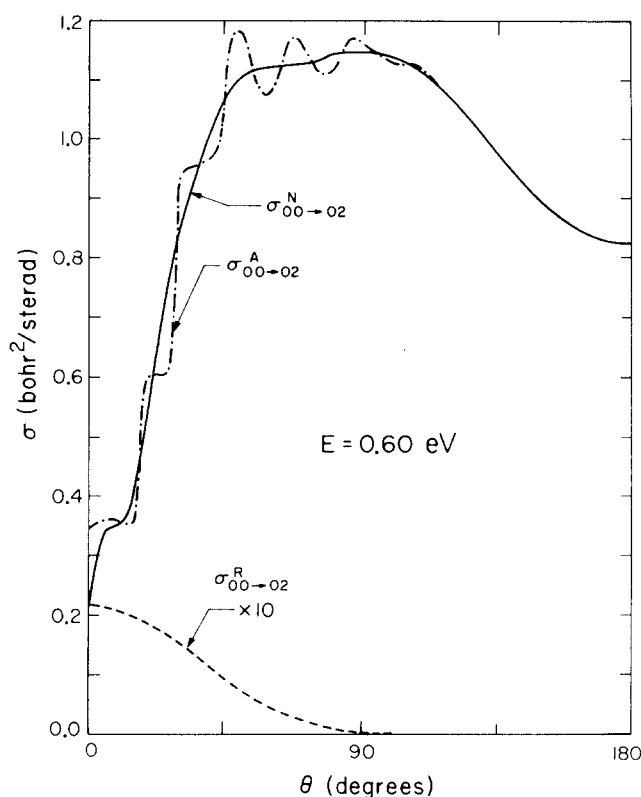


FIG. 13. Degeneracy-averaged  $\sigma_{00 \rightarrow 02}^N$ ,  $\sigma_{00 \rightarrow 02}^R$ , and  $\sigma_{00 \rightarrow 02}^A$  analogous to Fig. 11 but at  $E = 0.60$  eV ( $E_0 = 0.328$  eV).

scattering angles not too close to these directions. Since the  $j = 0$  to  $j' = 2$  transition can occur by both nonreactive and reactive mechanisms, the more meaningful quantity to consider is the antisymmetrized cross section of Eq. (2.8). In Figs. 12, 13, and 14 we plot this para-to-para cross section  $\sigma_{00 \rightarrow 02}^A$  (summed over  $m'_j$ ) along with the nonreactive and reactive counterparts at  $E = 0.5, 0.6,$  and  $0.7$  eV. At the lowest energy, the reactive cross section is typically 3 orders of magnitude smaller than the nonreactive one, so the resulting para-to-para cross section is dominated by the direct amplitude and differs very little from its nonreactive counterpart. As the energy is increased, the reactive amplitude increases rapidly and begins to interfere significantly with the nonreactive one. This results in the oscillations observed in  $\sigma_{00 \rightarrow 02}^A$  in Figs. 13 and 14. The period of these quantum symmetry oscillations seems to be roughly  $10^\circ - 15^\circ$  in both Figs. 13 and 14 for  $\theta < 90^\circ$  with a gradual increase in period with increasing  $\theta$  until the oscillations wash out completely at large  $\theta$ . Figures 12-14 also indicate that the peak in  $\sigma_{00 \rightarrow 02}^N$  shifts gradually to forward scattering angles (corresponding to backward reactive scattering angles) as the energy is increased. The contributions of different  $m'_j$  to  $\sigma_{00 \rightarrow 02}^A$  at  $0.7$  eV are shown in Fig. 15 (along with the distinguishable atom  $\sigma_{000 \rightarrow 02 m'_j}^N$  for comparison). We see that the oscillations in the cross section are largest for  $m'_j = 0$  followed by  $m'_j = \pm 1$  and  $m'_j = \pm 2$ . This results from the dominant role of the  $m'_j = 0$  reactive scattering amplitude (as evidenced in Fig. 10) followed in importance by the  $m'_j = \pm 1$  and the  $m'_j = \pm 2$  contributions. Note also that the phases of the oscillations in

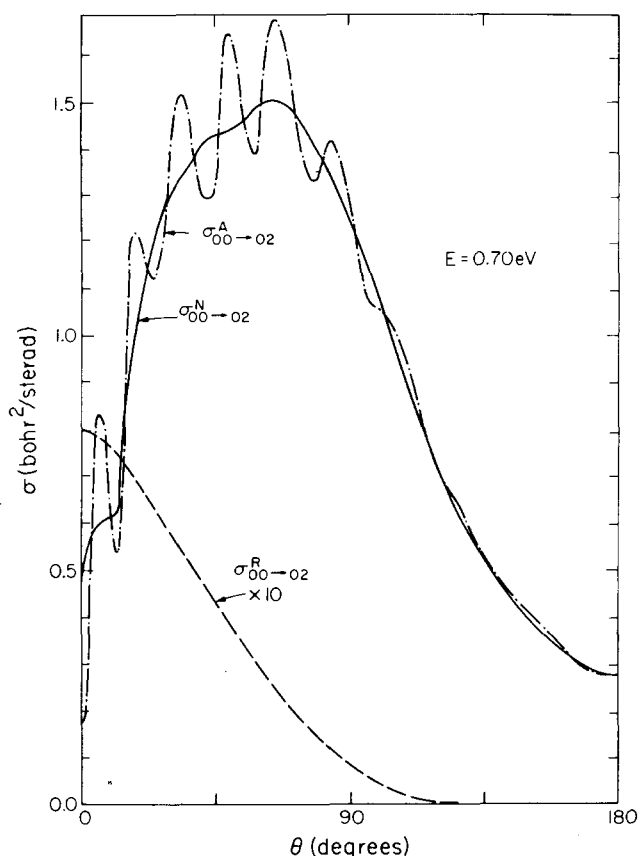


FIG. 14. Degeneracy-averaged  $\sigma_{00-02}^N$ ,  $\sigma_{00-02}^R$ , and  $\sigma_{00-02}^A$  analogous to Fig. 11 but at 0.70 eV ( $E_0 = 0.428$  eV).

Fig. 15(a), (b), and (c) are not particularly coherent, so that a certain amount of cancellation occurs in the sum over projections shown in Fig. 14.

### C. Integral cross sections and product polarization

A number of reactive, nonreactive and antisymmetrized integral cross sections are listed in Table V. Some of the reactive and para-to-ortho cross sections of that table are plotted as a function of energy in Fig. 16. Both logarithmic and linear scales are used to exhibit the tunnelling and the threshold regions. If we define the effective threshold energy  $E_T$  as that energy for which the cross section is  $0.05 \text{ bohr}^2$ , then  $E_T = 0.545$ ,  $0.550$ , and  $0.615$  eV for  $Q_{00}^R$ ,  $Q_{00-01}^A$ , and  $Q_{00-03}^A$ , respectively. Alternatively, since somewhat above the threshold region the energy dependence of the cross sections is linear, we could define an effective threshold energy  $E_T'$  as the energy at which a line fitted to the points in this linear region extrapolates to zero cross section. From this definition, we find  $E_T' = 0.568$ ,  $0.565$ , and  $0.605$  eV for these same cross sections, respectively. Either way we find that the threshold energies are considerably greater than the barrier height ( $0.396$  eV), and this fact will be discussed in detail in Sec. III E. At energies below the effective threshold, the effects of tunnelling give the cross section an approximately exponential dependence on translational energy  $E_0$ .

To examine the  $m_j$  dependence of the cross sections,

we list in Table VI a portion of the "cross section matrix"  $Q_{0jm_j-0j'm'_j}^R$  for  $j, j' \leq 2$  at  $0.6$  eV. (Note that these cross sections are distinguishable reactive ones.) The table indicates that the  $m_j = m'_j = 0$  cross section is typically 10–20 times larger than any other one with the same  $vj$  and  $v'j'$ . In addition, for given  $vjm_j$  and  $v'j'm'_j$ ,  $Q$  is a decreasing function of  $|m'_j|$  (and, by microscopic reversibility, for given  $vj$  and  $v'j'm'_j$ ,  $Q$  decreases with  $|m_j|$ ). These observations are indicative of the very significant product rotational angular momentum polarization effect that can occur when only a restricted range of collision geometries can lead to reaction. This approximate selection effect breaks down eventually for large enough  $j$  or  $j'$ . Let us consider the cross sections  $Q_{000-0j'm'_j}^R$  for varying  $j'$  and  $m'_j$  at  $0.6$  eV. The ratio of the  $m'_j = 0$  to the  $m'_j = \pm 1$  cross section is 22.3 for  $j' = 1$  decreasing to 7.1 for  $j' = 2$ , 3.1 for  $j' = 3$  and 1.1 for  $j' = 4$ . The  $j' = 1$  ratio is 10.6, 24.7, 24.9, 22.3, and 14.7 at  $E = 0.3, 0.4, 0.5, 0.6,$  and  $0.7$  eV, respectively, indicating that this selection rule is most rigorously obeyed in the range of energies just below the effective threshold. We shall examine the dependence of the degeneracy-averaged reactive integral cross sections on  $j$  and  $j'$  in Sec. III F.

The nonreactive degeneracy-averaged cross sections  $Q_{00-02}^N$  are listed in Table V. At  $0.6$  eV, the  $Q_{000-02m'_j}^N$

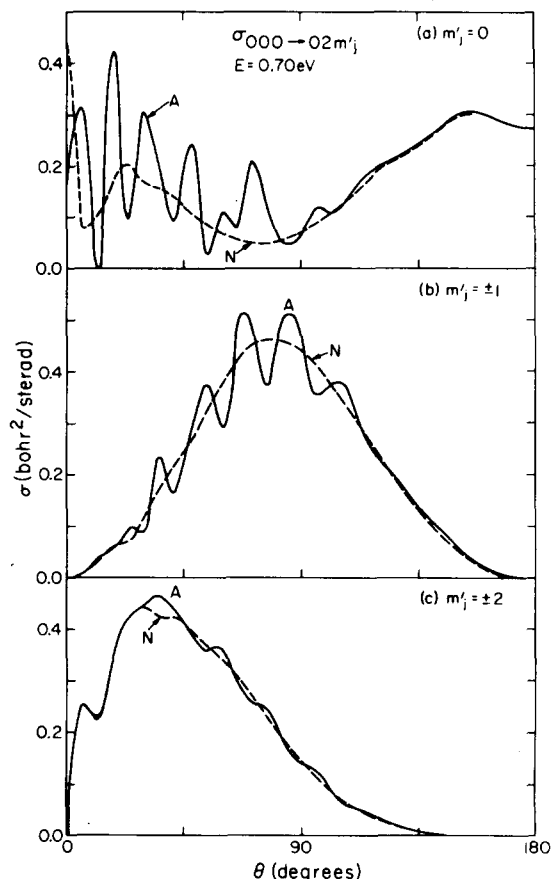


FIG. 15. Differential cross sections  $\sigma_{000-02m'_j}^A$  (solid lines labeled A) and  $\sigma_{000-02m'_j}^N$  (dashed lines labeled N) as a function of the scattering angle  $\theta$  for (a)  $m'_j = 0$ , (b)  $m'_j = \pm 1$ , and (c)  $m'_j = \pm 2$  at  $E = 0.70$  eV. The degeneracy-averaged results corresponding to these curves are shown in Fig. 14.

TABLE V. Integral cross sections at selected total energies.

Cross section <sup>a</sup> (bohr <sup>2</sup> )	Total energy (eV)								
	0.30	0.35	0.40	0.45	0.50	0.55	0.60	0.65	0.70
$Q_{00-01}^A$	0.388(-13)	0.360(-8)	0.200(-5)	0.141(-3)	0.372(-2)	0.0400	0.234	0.571	0.905
$Q_{00-03}^A$	b	b	0.410(-8)	0.241(-5)	0.166(-3)	0.346(-2)	0.0295	0.104	0.222
$Q_{00-ortho}^A$	0.388(-13)	0.360(-8)	0.201(-5)	0.144(-3)	0.390(-2)	0.0435	0.264	0.676	1.13
$Q_{02-ortho}^A$	b	0.916(-10)	0.149(-6)	0.183(-4)	0.628(-3)	0.910(-2)	0.0632	0.209	0.423
$Q_{04-ortho}^A$	b	b	b	0.289(-8)	0.218(-5)	0.478(-3)	0.131(-2)	0.0155	0.0269
$Q_{00}^R$	0.156(-12)	0.480(-8)	0.252(-5)	0.184(-3)	0.501(-2)	0.0574	0.352	0.933	1.52
$Q_{01}^R$	0.232(-13)	0.205(-8)	0.130(-5)	0.106(-3)	0.306(-2)	0.0372	0.228	0.648	1.11
$Q_{02}^R$	b	0.120(-9)	0.186(-6)	0.234(-4)	0.806(-3)	0.0120	0.0843	0.291	0.575
$Q_{03}^R$	b	b	0.333(-8)	0.145(-5)	0.908(-4)	0.196(-2)	0.0166	0.0677	0.160
$Q_{04}^R$	b	b	b	0.371(-8)	0.289(-5)	0.700(-3)	0.179(-2)	0.0224	0.0484
$Q_{00-02}^N$	b	d	3.00	d	8.82	d	13.0	d	13.2
$Q_{00-02}^R$	b	0.595(-10)	0.114(-6)	0.142(-4)	0.473(-3)	0.643(-2)	0.0437	0.130	0.220
$Q_{00-02}^A$	b	d	3.00	d	8.82	d	13.0	d	13.5
$Q_{00-00}^N$	299 <sup>c</sup>	d	260 <sup>c</sup>	d	234 <sup>c</sup>	d	217 <sup>c</sup>	d	205 <sup>c</sup>

<sup>a</sup>All cross sections have been degeneracy averaged. Those para-to-ortho cross sections which have been summed over final states are only summed over those final states of the correct spin symmetry. Numbers in parentheses indicate the power of 10, by which the numbers preceding them should be multiplied.

<sup>b</sup>Transition is energetically forbidden.

<sup>c</sup>Obtained by the extrapolation procedure of Sec. III D.

<sup>d</sup>Calculation not done.

have values of 3.01, 3.31, and 1.67 bohr<sup>2</sup> for  $m_j = 0, \pm 1$ , and  $\pm 2$ , respectively, which is indicative of the lack of strong rotational angular momentum polarization effects such as are observed for the reactive cross sections. The reason, as pointed out previously, is the lack of linear or near linear orientation restrictions for nonreactive rotationally inelastic collisions. Table V also indicates that  $Q_{00-02}^N$  and  $Q_{00-02}^A$  are equal (within the accuracy of the calculation) except at the highest energy considered. An additional discussion of the energy dependence of these nonreactive cross sections is given in Sec. III G.

#### D. Elastic and total cross sections

The calculation of converged elastic cross sections requires a large number of partial waves (up to 70 at 0.70 eV). Since the Porter-Karplus surface has a repulsive exponential long-range functionality<sup>2c</sup> rather than the correct attractive  $R_\lambda^{-6}$  dependence<sup>40</sup> a fully coupled calculation of the elastic cross sections for the purpose of comparison with experiments<sup>40</sup> on this and related systems would not be worthwhile without inclusion of this attractive tail in the potential. Nevertheless, an accurate calculation of the elastic differential

TABLE VI. Integral reactive cross sections  $Q_{v'j'm'_j-vj'm_j}^R$  (in bohr<sup>2</sup>) at  $E=0.60$  eV.<sup>a</sup>

$v'j'm'_j$									
$vjm_j$	000	011	010	01-1	022	021	020	02-1	02-2
000	0.0432	0.00322	0.0717	0.00322	0.227(-3)	0.00474	0.0338	0.00474	0.227(-3)
011	0.00337	0.549(-3)	0.00596	0.835(-3)	0.488(-4)	0.709(-3)	0.00261	0.00127	0.774(-4)
010	0.0751	0.00596	0.128	0.00596	0.380(-3)	0.00812	0.0578	0.00812	0.380(-3)
01-1	0.00337	0.835(-3)	0.00596	0.549(-3)	0.774(-4)	0.00127	0.00261	0.709(-3)	0.488(-4)
022	0.262(-3)	0.538(-4)	0.419(-3)	0.855(-4)	0.111(-4)	0.811(-4)	0.209(-3)	0.134(-3)	0.146(-4)
021	0.00549	0.783(-3)	0.0089	0.00140	0.811(-4)	0.00113	0.00407	0.00228	0.134(-3)
020	0.0391	0.00288	0.0638	0.00288	0.209(-3)	0.00407	0.0286	0.00407	0.209(-3)
02-1	0.00549	0.00140	0.00897	0.783(-3)	0.134(-3)	0.00228	0.00407	0.00113	0.811(-4)
02-2	0.262(-3)	0.855(-4)	0.419(-3)	0.538(-4)	0.146(-4)	0.134(-3)	0.209(-3)	0.811(-4)	0.111(-4)

<sup>a</sup>All reactance matrices have been symmetrized [see Ref. 14(a)] before the above cross sections were calculated. Numbers in parentheses indicate the power of 10 by which the numbers preceding them should be multiplied.

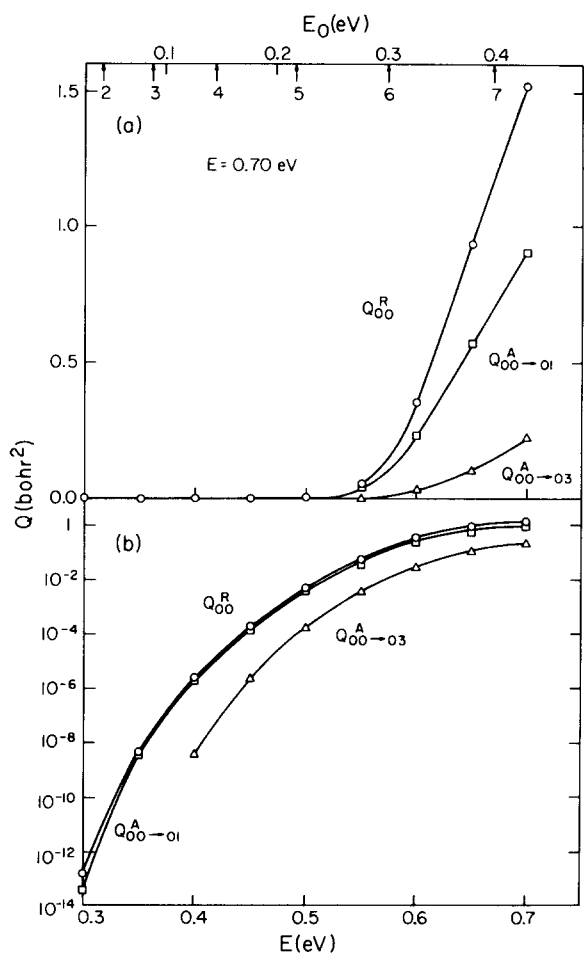


FIG. 16. Integral cross sections  $Q_{00}^R$ ,  $Q_{00}^{A-01}$ , and  $Q_{00}^{A-03}$  (degeneracy averaged) as a function of the total energy  $E$  and translational energy  $E_0$ . Arrows in upper abscissa indicate the energies at which the rotational states  $j=2-7$  (for  $v=0$ ) of  $H_2$  become energetically accessible: (a) linear scale, (b) logarithmic scale.

and integral cross sections for this Porter-Karplus surface is still worthwhile in order to provide a comparison standard for approximate techniques used in calculating these same cross sections, such as the central field approximation being invoked in the interpretation of molecular beam scattering experimental data.<sup>41,42</sup> This requires the calculation of the scattering matrix element phases for very large  $J$ . We found a very accurate extrapolation procedure which could be used to obtain these phase shifts. For  $J$  large enough so that both reactive and inelastic nonreactive transition probabilities are negligible, it is often the case that the elastic phase shifts have not yet decayed to zero. Since these large  $J$  collisions correspond to large impact parameters, we would expect that only the isotropic tail of the potential is important. In such circumstances, a central field, single channel model of the potential should suffice to predict these phase shifts. Using a standard central potential integration routine<sup>43</sup> with the spherically averaged potential  $V_0(r_e, R)$  of Eq. (2.14), where  $r_e$  is the equilibrium internuclear distance, we have calculated the elastic  $v=j=0$  phase shifts at the energies considered in Table V. Typical results are

presented in Fig. 17, where we have also plotted the phase shift of the exact scattering matrix elements  $[\frac{1}{2} \arg(S_{J,000-000}^N)]$ . The figure indicates that the accurate phase shifts are essentially identical to their central field counterparts for  $J > 10$ . Indeed, between  $J=11$  and  $J=39$  (the highest  $J$  for which a fully coupled calculation was done), the difference between these two phase shifts is always less than 0.05 rad and usually less than 0.02 rad. This is rather interesting, since at  $J=11$  the modulus of  $S_{J,000-000}^N$  (equal to  $[P_{J,000-000}^N]^{1/2}$ ) is not even close to unity, as is illustrated in Fig. 17. This presumably indicates that the phases of the scattering matrix elements are much less sensitive to the presence of reactive and inelastic channels than are the moduli. By using these elastic central field phase shifts, we can now extrapolate the large  $J$  behavior of the converged results and thus calculate accurate elastic cross sections.<sup>44</sup> Typical results for  $\sigma_{000-000}^N$  at  $E=0.7$  eV are plotted in Fig. 18. The elastic differential cross section shows strong forward peaking with a small oscillation near  $\theta=6^\circ$  and otherwise decreases in a nearly monotonic manner to  $\theta=180^\circ$ . The indicated  $\theta=110^\circ$  to  $180^\circ$  behavior of  $\sigma_{000-000}^N$  is probably not accurate since the small cross sections in this region must result from extensive cancellation in the partial wave sum [Eq. (2.2)] and are easily affected by small errors in the scattering matrix elements. Also plotted on the same graph are the central field elastic cross section  $\sigma^E(\text{CF})$  [obtained using  $V_0(r_e, R)$  for all  $J$ ] and the total cross section  $\sigma_{000}^T$  [which is the sum of the cross sections for all possible processes ( $N$  or  $R$ ) starting from reagents  $v=j=m_j=0$ ]. We see that all three cross sections are essentially identical for  $\theta < 30^\circ$ . This suggests that the central field approximation used to interpret total differential cross sections<sup>41</sup> out to scattering angles which are not too large is a good one. Even for very large scattering angles  $\sigma_{000}^T$  and  $\sigma^E(\text{CF})$  agree to within better than a factor of 2. Moreover, the integral cross sections  $Q_{000}^T$  and  $Q^E(\text{CF})$  are 221.0 bohr<sup>2</sup> and

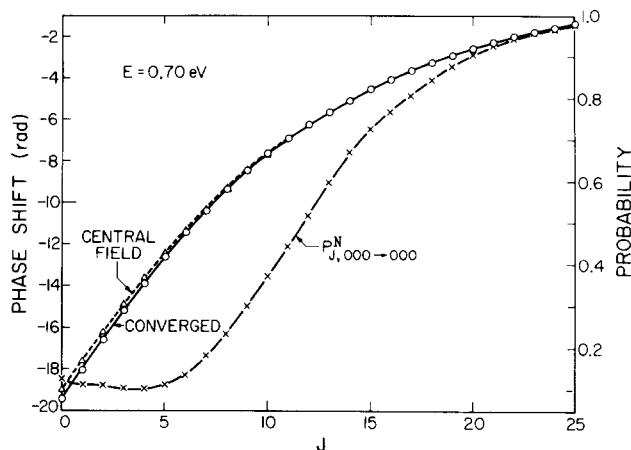


FIG. 17. Phase shift associated with the elastic scattering matrix element  $S_{J,000-000}^N$  (i. e.,  $[\arg(S_J)]/2$ ) as a function of  $J$  for  $E=0.70$  eV. Curve labeled converged is the coupled-channel result, while the central field curve is the result of a single channel calculation described in text. Also plotted is the (converged) elastic transition probability  $P_{J,000-000}^N$  at the same energy referenced to right hand ordinate scale.

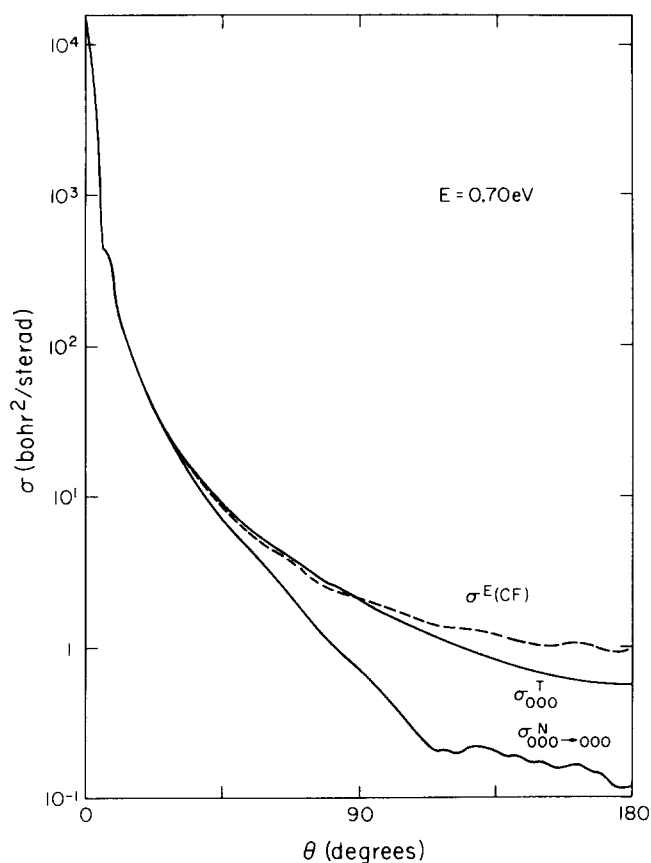


FIG. 18. Elastic differential cross section  $\sigma_{000-000}^N$  and total cross section  $\sigma_{000}^T$  (both obtained from the coupled-channel calculation), along with the central field elastic cross section  $\sigma^{E(CF)}$  as a function of scattering angle at  $E = 0.70$  eV.

220.8 bohr<sup>2</sup>, respectively, indicating that Levine's conservation of total cross section rule<sup>45</sup> is obeyed quite accurately for this system and that the use of the central field approximation to interpret total cross section experiments<sup>42</sup> is valid. The  $H + H_2$  total cross section just mentioned is considerably larger than the recently measured experimental one<sup>40</sup> (for  $D + H_2$ ), which is about 151 bohr<sup>2</sup> at 0.75 eV. This is probably due to differences between the long-range parts of the Porter-Karpus and correct potential energy surfaces.

If the antisymmetrized cross section  $\sigma_{000-000}^A$  is considered, we find that quantum symmetry effects due to interference between the elastic and reactive scattering amplitudes are much less significant than they were with the inelastic transitions in Fig. 14. Nevertheless, oscillations in this cross section can result in differences between  $\sigma^A$  and  $\sigma^N$  as big as 10% of  $\sigma^N$  for scattering angles between 30° and 90°.

### E. Comparison of collinear, coplanar, and three dimensional results

In the analysis of the coplanar results,<sup>13b</sup> it was determined that a physically meaningful comparison of the 1D and 2D results could be obtained by examining the  $J=0$  total reaction probabilities. We extend this comparison in Figs. 19 and 20 by plotting the 1D,<sup>21,46</sup> 2D, and 3D total reaction probabilities  $P_{00}^R(J=0)$  [ $P_0^R$  for 1D]

as a function of  $E$ . Both logarithmic and linear scales are used so as to enable examination over a wide energy range. The figures indicate a surprisingly similar energy dependence over several orders of magnitude of the probabilities. There are, however, two important differences both of which provide significant insight into the reactive collision dynamics. First, an energy shift of about 0.05 eV occurs in going from 1D to 2D and again in going from 2D to 3D. In the coplanar analysis,<sup>13b</sup> we explained the 1D to 2D shift as arising from an additional bending energy required in the coplanar transition state over the linear one. This bending energy is added to the symmetric stretch energy of the collinear transition state which, in turn, is primarily responsible for the shift in the collinear effective threshold energy over the barrier height energy<sup>14</sup> (0.396 eV). In the three-dimensional case, the bending mode of the transition state is doubly degenerate so that a second quantum of bending energy (approximately equal to the bending zero point energy of about 0.06 eV) will be required. Indeed, an examination of Fig. 19 indicates that the 1D to 2D and 2D to 3D energy shifts for  $P^R = 0.01$  are identical to within the accuracy to which

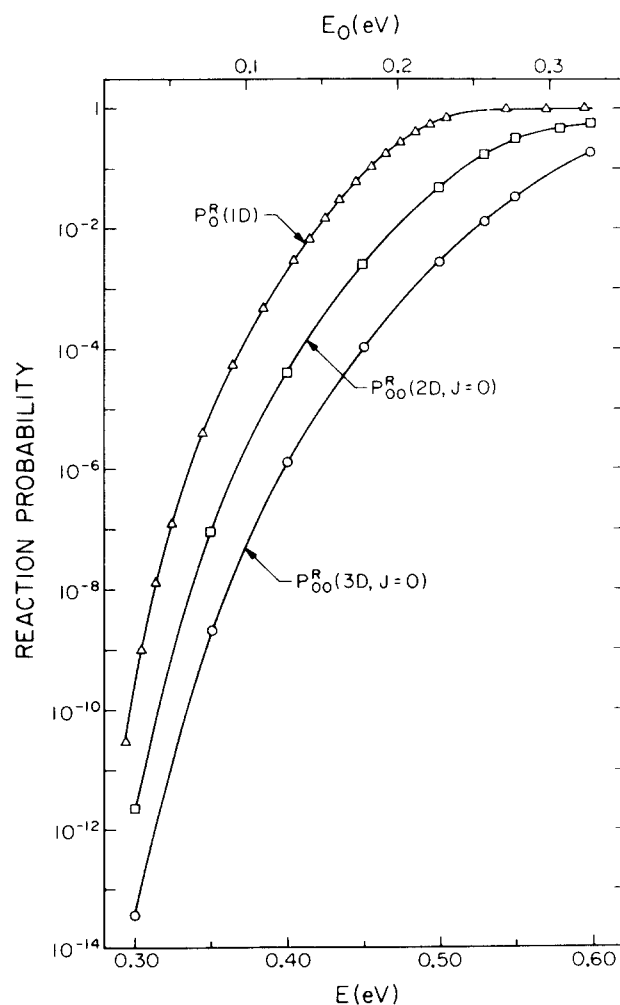


FIG. 19. One-, two-, and three-dimensional total reaction probabilities  $P_{00}^R(1D)$ ,  $P_{00}^R(2D, J=0)$ , and  $P_{00}^R(3D, J=0)$ , summed over all final states, as a function of the total energy  $E$  and translational energy  $E_0$ .

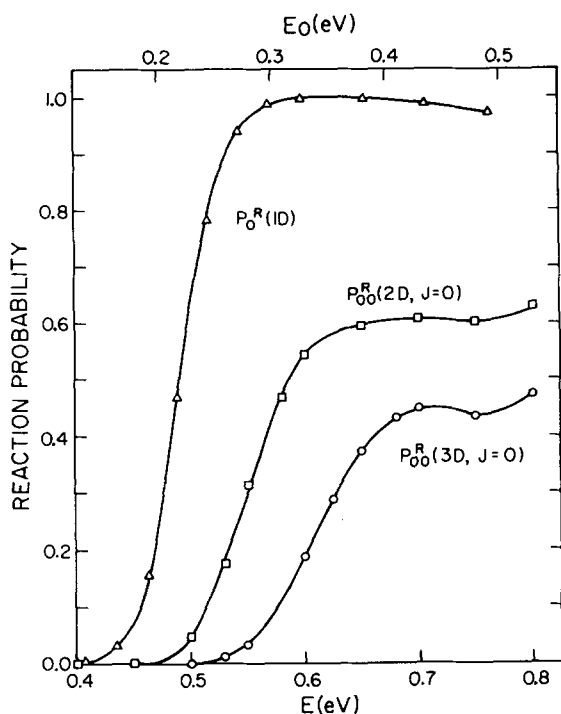


FIG. 20. One-, two-, and three-dimensional total reaction probabilities analogous to Fig. 19 but with a linear rather than logarithmic ordinate scale.

the probabilities can be interpolated. The second difference between 1D, 2D, and 3D results lies in the magnitudes of the maximum probabilities in Fig. 20. The collinear probability peaks near unity while the planar one levels off at about 0.6, and the 3D one roughly at 0.45. The difference between the 1D and 2D plateau values has been previously analyzed<sup>13b</sup> in terms of the orientation dependence of the 2D probability. Since the potential barrier varies from 0.396 eV at  $\gamma_\lambda = 0$  to 2.8 eV at  $\gamma_\lambda = 90^\circ$ ,<sup>2c</sup> one would expect a decreasing probability of reaction with increasing  $\gamma_\lambda$  (assuming that we can consider the orientation of the atom with respect to the diatom as fixed throughout the reaction). If we consider that the total reaction probability is unity for  $0 \leq \gamma_\lambda \leq \bar{\gamma}_\lambda$  and zero for  $\bar{\gamma}_\lambda \leq \gamma_\lambda \leq 90^\circ$ , and use symmetry about  $90^\circ$  for  $90^\circ \leq \gamma_\lambda \leq 180^\circ$ , then we find that  $P_{00}^R(2D) = 2\bar{\gamma}_\lambda/\pi$  and  $P_{00}^R(3D) = 1 - \cos\bar{\gamma}_\lambda$ . In the 2D case, we find that  $\bar{\gamma}_\lambda = 54^\circ$  is required to give a reaction probability of 0.6. This estimate of  $\bar{\gamma}_\lambda$  is in approximate agreement with previous estimates of this angle from a classical analysis.<sup>3</sup> The same angle used in the 3D formula yields  $P_{00}^R(3D) = 0.41$  which is not considerably different from the observed value of 0.45. This indicates that the 2D and 3D orientation dependence is probably quite similar with primarily dimensionality considerations responsible for the difference in reaction probabilities.

At least two procedures for converting 2D integral or differential cross sections into 3D ones have been proposed<sup>11,47</sup> both of which use semiclassical arguments in making the connection. We will leave for future publications a thorough analysis of these conversion procedures as well as an evaluation of approximate 3D procedures which require comparable or smaller amounts of com-

putation time than the 2D calculation while providing 3D information directly. We would like to point out, however, one rather remarkable comparison between 2D and 3D results which is obtained by examining the differential cross sections. In Fig. 21 we plot the 2D and 3D differential cross section  $\sigma_{00-01}^A$  (adjusting the respective ordinate scales to bring them into approximate agreement at  $\theta_R = 180^\circ$ ). The 2D result at 0.55 eV is compared to the 3D one at 0.60 eV so as to include the energy shift effect due to the bending energy.

These two cross sections show a remarkably similar angular dependence over the entire range of scattering angles. A similar comparison at other energies in the range considered in this paper usually leads to comparable agreement. This indicates that the dynamical processes involved are indeed quite similar. Such behavior is not unexpected, for the same potential is sampled in both cases and the primary difference between the two calculations is the additional centrifugal coupling resulting from tumbling of the three-atom plane, which is present in 3D but not in 2D. The existence of a strong rotational polarization selection effect as evidenced in Table VI indicates that such coupling is weak in comparison to the potential coupling since it is the potential which is responsible for the linear geometry requirement. Thus 2D and 3D dynamics should be quite similar and conversion of 2D to 3D results could prove to be an accurate approximate technique.

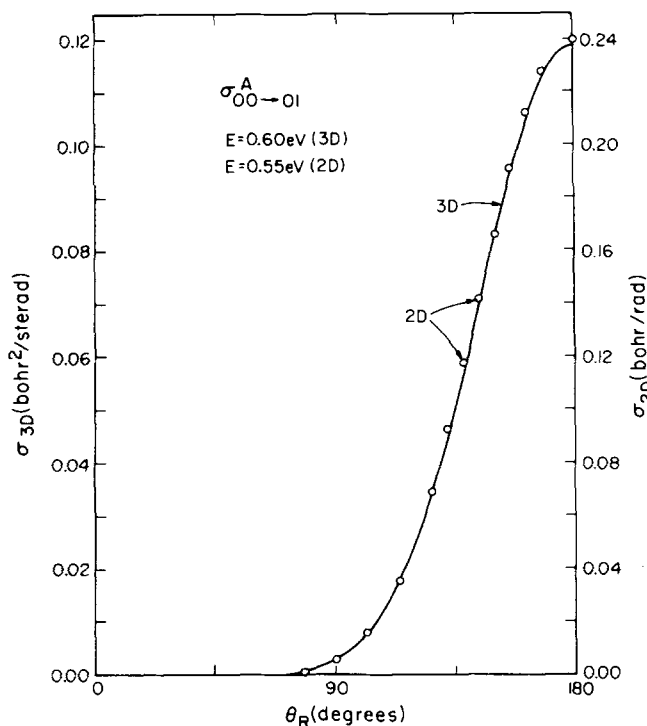


FIG. 21. Two- and three-dimensional differential cross sections  $\sigma_{00-01}^A(2D)$  [Ref. 13(b)] and  $\sigma_{00-01}^A(3D)$  as a function of reactive scattering angle  $\theta_R$ . The 3D cross section (solid curve), at 0.60 eV total energy, is referenced to the left side ordinate scale while the 2D result (circles) at 0.55 eV is referenced to the right side one.

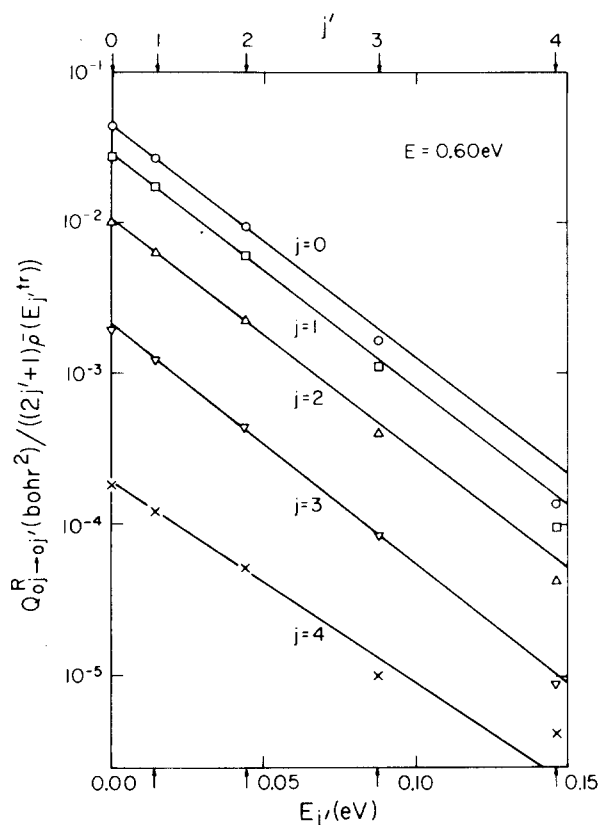


FIG. 22. Reactive degeneracy-averaged integral cross sections  $Q_{0j \rightarrow 0j'}^R$ , divided by  $(2j' + 1) \bar{\rho}(E_j^{tr})$ , as a function of the product rotational energy  $E_{j'}$ , and rotational quantum number  $j'$  at 0.60 eV total energy for initial rotational quantum numbers  $j = 0-4$ .

#### F. Reagent and product rotational state distributions

We now consider the rotational distributions of the degeneracy-averaged reactive distinguishable atom cross sections (all for  $v = v' = 0$ ). In the coplanar H + H<sub>2</sub> study,<sup>13b</sup> we found that a surprisingly accurate fit to this distribution could be obtained with a temperaturelike expression (for a 2D system). This type of distribution can be derived from an information theoretic formalism through the assumption that the surprisal function<sup>48</sup> is a linear function of the final state rotational energy. For 3D collisions, with only one open vibrational channel, the information theoretic expression for the degeneracy-averaged cross section between rotational states  $j$  and  $j'$  may be written as

$$Q_{j \rightarrow j'}^R = A_j(E) \rho(E_j^{tr}) (2j' + 1) e^{-E_{j'}/kT_j(E)}, \quad (3.1)$$

where the pre-exponential factors comprise the reference or statistical distribution, and  $T_j$  and  $A_j$  are the two  $j'$ -independent parameters of the theory.  $\rho(E_j^{tr})$  is the product translational density of states and is a function of the translational energy  $E_j^{tr}$  relative to state  $j'$ .  $E_{j'}$  is the product rotational energy, so that  $E_j^{tr} = E - E_{j'} - E^0$ , where  $E^0$  is the  $v' = j' = 0$  zero point energy. The  $2j' + 1$  in Eq. (3.1) is the product rotational degeneracy factor. To see how well our 3D cross sections obey Eq. (3.1), we have plotted in Fig. 22 the cross sections  $Q_{0j \rightarrow 0j'}^R$  divided by  $(2j' + 1) \bar{\rho}(E_j^{tr})$  on a logarithmic scale as a function of  $E_{j'}$  for several initial states  $j$  at 0.6 eV,

where  $\bar{\rho}(E_j^{tr}) = \rho(E_j^{tr}) / \rho(E - E^0)$  so that for  $E_{j'} = 0$ ,  $\bar{\rho} = 1$ . If Eq. (3.1) is satisfied, then the resulting curves should be linear with slopes inversely proportional to  $T_j(E)$ . We see from the figure that the calculated points for low  $j'$  do indeed fall on nearly straight lines for each  $j$ , thus indicating that the temperaturelike distribution is quite accurate for describing the reactive cross sections. The temperature parameters obtained from these low  $j'$  straight lines are 326, 326, 328, 318, and 376 K for  $j = 0, 1, 2, 3$ , and 4, respectively. The first four values are identical to one another within the accuracy of the straight line fits. Actually, one can easily show by applying microscopic reversibility to Eq. (3.1) that if the rotational distribution is temperaturelike for all  $j$  then  $T_j(E)$  must be independent of  $j$ , which can be written simply as  $T(E)$ . The above listed temperatures should therefore all be the same if the distributions are truly temperaturelike. Only for  $j = 4$  or  $j' = 4$  are deviations from temperaturelike behavior significant. If we now perform a similar analysis at several other total energies we obtain Fig. 23 which depicts the  $j = 0$  distributions between 0.45 and 0.70 eV. Temperaturelike behavior is evident to a comparable extent at all energies considered. The temperature parameters obtained from the slopes of the lines in Fig. 23 vary from 228 K to 446 K as  $E$  varies from 0.45 eV to 0.70 eV in steps of roughly 40 K/0.05 eV increase in energy.

As pointed out by Wyatt,<sup>49</sup> these temperaturelike pa-

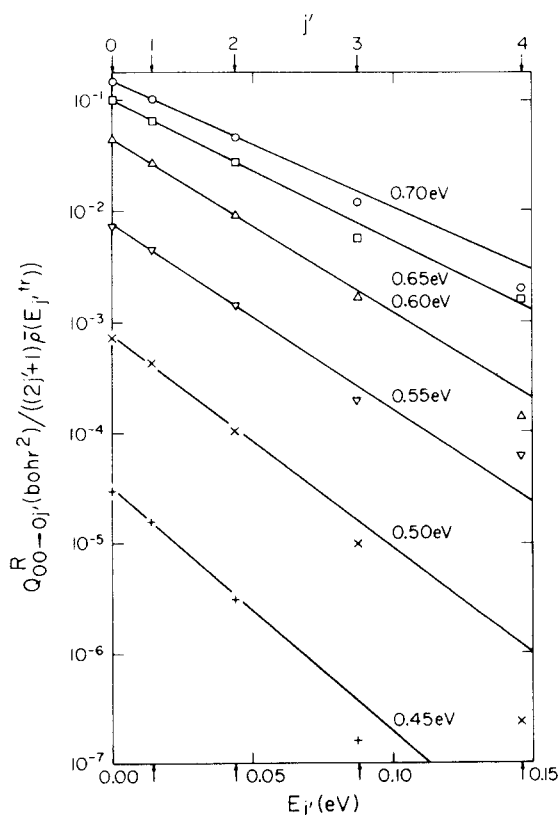


FIG. 23. Reactive degeneracy-averaged integral cross sections  $Q_{00 \rightarrow 0j'}^R$ , divided by  $(2j' + 1) \bar{\rho}(E_j^{tr})$ , as a function of the product rotational energy  $E_{j'}$ , and rotational quantum number  $j'$  at 0.45, 0.50, 0.55, 0.60, 0.65, and 0.70 eV total energy.

rameters should *not* be interpreted as being equal to the temperature of a canonical ensemble describing a thermal equilibrium between a bath and the products of the reaction (which actually belong to a nonequilibrium microcanonical ensemble). Under conditions leading to product population inversions, Eq. (3.1), when satisfied, furnishes negative  $T_j(E)$ . We have expressed the present reaction product rotational population results in terms of temperaturelike parameters because the latter turned out to be positive and a quantitative feeling for the relative population of the product states is immediately conveyed by reporting their values. An alternative but equivalent procedure is to express the results in terms of the slopes  $\theta(E)$  of the linear surprisal plots.<sup>48,49</sup> It is easy to show that  $\theta(E)$  is related to  $T(E)$  by  $\theta(E) = (E - E^{v'})/[kT(E)]$ , where  $E^{v'}$  is the vibrational energy of the products whose rotational population is being considered. In the present instance  $E^{v'}$  is the zero-point vibrational energy of  $H_2$  and the surprisal slope parameters  $\theta(E)$  corresponding to Fig. 23 vary from 9.1 at  $E=0.45$  eV to 11.1 at  $E=0.70$  eV in a non-linear manner. The results obtained by Wyatt<sup>49</sup> for an approximate version of the Yates-Lester-Liu (YLL) potential energy surface<sup>21,50</sup> furnish  $\theta=8.9$  for  $E=0.70$  eV and 0.80 eV. The difference between these results may be attributed in part to the difference between the YLL<sup>50</sup> and PK<sup>2c</sup> surfaces and in part to the difference between the methods used in the scattering calculations (see Sec. III G).

In the coplanar study<sup>13b</sup> we pointed out that the existence of temperaturelike rotational distributions could be a reflection of the shape of the potential energy surface near the transition state and the significant restriction in bending motions which the potential induces there. Since the transition state bending motions correlate adiabatically with asymptotic free rotor motions one might expect that the average rotational energy of the products should be related to the average energy in bending. This relation does not seem to be quantitative, however, for the average product state rotational energy corresponds roughly to the temperature parameter while the bending energy, as estimated in the previous section, seems to be somewhat higher (228–446 K for the former and 550 K for the latter). The model explains the similarity between the coplanar and three-dimensional temperature parameters (311 K for 2D<sup>13b</sup> vs 326 K for 3D, both at 0.6 eV) only if we further assume that only one of the two degenerate 3D bending modes becomes product rotational motion. This assumption disagrees with the interpretation given above for the energy shifts of Figs. 19 and 20. It therefore appears that some refinement in the model which relates product rotational energies to transition state bending energies is necessary in order to quantitatively explain the temperature parameters obtained from the distributions of Figs. 22 and 23.

### G. Comparisons with the results of other three dimensional calculations

In Figs. 24 and 25 we compare our integral cross sections (labeled SK) with the corresponding ones obtained by several other methods, all applied to  $H+H_2$  on

the Porter-Karplus potential surface. In Fig. 24 we plot the quasiclassical total reactive cross sections of Karplus, Porter, and Sharma<sup>3</sup> (KPS) and the quantum mechanical results of Elkowitz and Wyatt<sup>10</sup> (EW), while Fig. 25 contains the antisymmetrized distorted wave  $Q_{00-01}^A$  results of Tang and Karplus<sup>5</sup> (TK) and of Choi and Tang<sup>8</sup> (CT) and the one-vibration close-coupling results of Wolken and Karplus<sup>7</sup> (WK).

It is apparent that the best agreement in either figure is between our  $Q_{00}^R$ (SK) and  $Q_{01}^R$ (SK) and the corresponding quasiclassical quantities. Our converged quantum result and the quasiclassical cross sections are essentially identical between 0.6 and 0.7 eV to within the statistical accuracy of the quasiclassical calculation. Agreement between  $Q_{02}^R$ (SK) and  $Q_{02}^R$ (KPS) is much less quantitative but still reasonable if one considers the small cross sections involved and the inherent statistical uncertainty in the quasiclassical result. Below the classical thresholds, we observe characteristic tunneling behavior in our quantum cross sections which will have an important effect in the comparison of classical

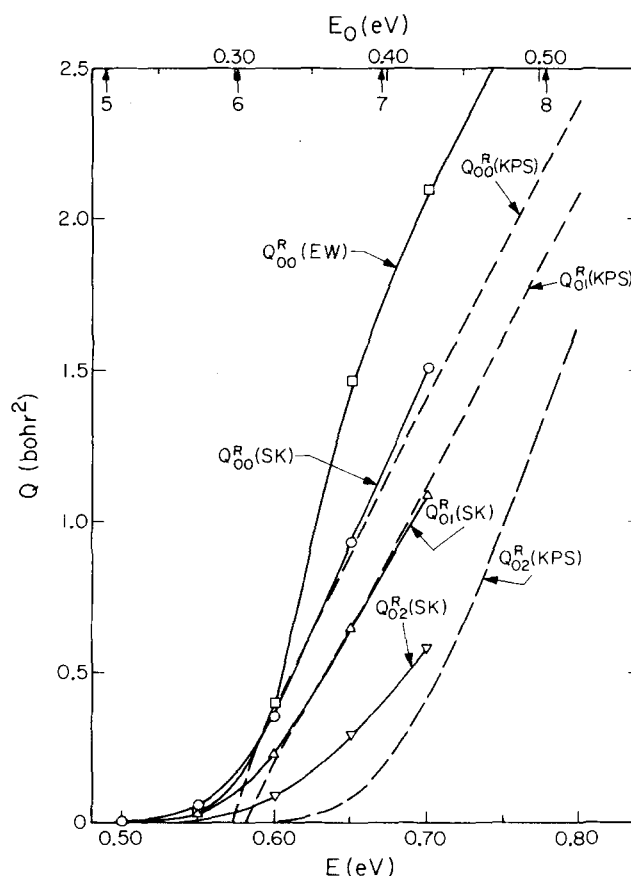


FIG. 24. Comparison of reactive integral cross sections as a function of the total energy  $E$  for several calculations. The  $Q_{0j}^R$ (KPS) for  $j=0, 1$ , and 2 are the quasiclassical results of Karplus, Porter, and Sharma (indicated by dashed lines), while  $Q_{00}^R$ (EW) is the analogous total reaction cross section obtained by Elkowitz and Wyatt (indicated by squares). The present results are connected by solid lines and labeled  $Q_{0j}^R$ (SK) with  $j=0, 1, 2$ . The arrows below the upper abscissa indicate the energies at which the ground vibrational state product rotational levels having the  $j$  values indicated become energetically accessible.

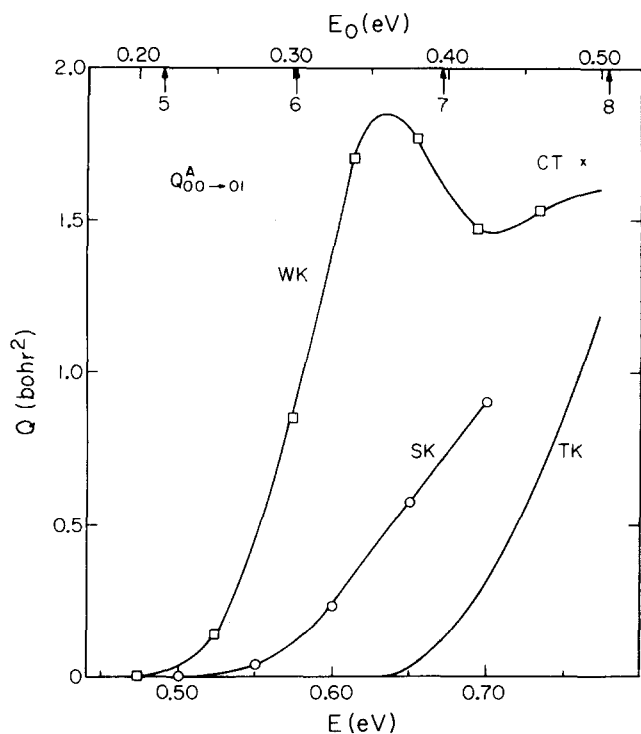


FIG. 25. Comparison of the integral cross sections  $Q_{00}^A \rightarrow 01$  as a function of  $E$ . The results labeled WK are those of Wolken and Karplus, TK denotes those of Tang and Karplus, CT the one point of Choi and Tang, and SK the present results. The TK results in Ref. 5 have been multiplied by the necessary factor of 3 to obtain the curve plotted. The arrows below the upper abscissa have the same meaning as in Fig. 24.

and quantum thermal rate constants (see Sec. III H).

Agreement between our results and the corresponding one of Elkowitz and Wyatt<sup>10</sup>(EW) is not as good as one would have expected considering that both calculations were done on the same potential energy surface and they both employed extended vibration-rotation basis sets. Recently, EW have made some corrections in their calculations<sup>51</sup> which improve the agreement between their  $Q_{00}^R$  curve and ours. In addition, over the energy range 0.6–0.7 eV, the corrected EW values for  $Q_{00}^A \rightarrow 01$  agree with ours to within 20%. On the other hand, their  $Q_{00}^A \rightarrow 03$  are about 2.5 times greater than ours, and as a result, when we compare the cross section ratios  $Q_{00}^A \rightarrow 03 / Q_{00}^A \rightarrow 01$  from Table V with the corresponding ones from Fig. 1(a) of Ref. 10 or with EW corrected values,<sup>51</sup> we find that the difference between them is quite large. For example, at  $E = 0.70$  eV we get 0.24 for that ratio, whereas the EW value is 0.62. This implies that the distribution of energy among the rotational degrees of freedom of the products is very different in both calculations, and that the temperaturelike parameters which may result from their calculations will be significantly larger than the ones reported in the previous section. A search is presently going on for the reasons for this difference in the cross sections. In this context it should be noticed that EW simplified their calculation in three ways,<sup>52</sup> one or more of which could have an appreciable effect on the results, particularly at large energies: (a) They omitted certain Coriolis

coupling terms from the kinetic energy part of the Hamiltonian; (b) The potential was fitted to analytic expressions whose form was chosen so as to omit vibration-rotation coupling; and (c) Only the  $v = 0, 1, 2$  vibrational states were included in the coupled-channel expansion and convergence with respect to the number of vibrational states was not tested. In our case, as pointed out in Sec. II B, Table III, and in Ref. 13, usually four vibrational basis functions were required for convergence of the reaction probabilities to a few percent.

The Tang and Karplus distorted wave curve in Fig. 25 has a much higher effective threshold energy than ours and consequently much smaller cross sections at the same energy. Part of the difficulty could be the “linear” assumption used<sup>5</sup> in evaluating the integrals for the transition amplitude. When this assumption was removed, as was done by Choi and Tang,<sup>8</sup> the cross section increased significantly at the one energy they considered. We should also note that Choi and Tang<sup>8b</sup> have also observed an  $m'_j$  dependence in their  $P_{J, 000-01}^R$ ; reaction probabilities quite similar to that of Fig. 3. It would be interesting to obtain distorted wave results such as those of CT at lower energies so that a more direct comparison with our results may be made. The one vibrational basis function results of Wolken and Karplus<sup>7</sup> have an effective threshold energy much lower than ours for the same transition. This is probably a consequence of the severely truncated basis set used (only vibrational quantum state  $v = 0$  and the  $j = 0-3$  rotational states). Convergence properties of such severely truncated basis sets were examined in the coplanar  $H + H_2$  study,<sup>13b</sup> and it was determined there that errors of several orders of magnitude in cross sections were possible in some cases if both vibrational and rotational convergence was not achieved.

The quasiclassical and quantum differential cross sections  $\sigma_{00}^R$  (at somewhat different energies) are examined in Fig. 26. Both angular distributions are backward peaked with very similar shapes. A very interesting comparison between classical and quantum dynamics would involve an examination of the classical rotational polarization effect analogous to the one found in the quantum results and displayed in Fig. 10. Such a detailed comparison of cross sections between individual quantum states (rather than summed over several as is the case in Figs. 24 and 26) would be highly desirable in establishing the general validity of the quasiclassical procedure. Figure 27 provides a comparison of the WK, CT, and SK  $\sigma_{00}^A \rightarrow 01$  angular distributions at similar energies. We find the shape of the distorted wave differential cross section curve of Choi and Tang to be very similar to ours, while that of the Wolken and Karplus cross section differs rather substantially from either. Part of the error in the WK result could be due to an ambiguity in the interpolation of amplitudes and phases of scattering matrix elements for those partial waves they did not explicitly calculate. (Only every third partial wave was calculated.)<sup>7</sup> Indeed, we have found interpolation procedures to be extremely dangerous (especially for the phases), and for this reason,

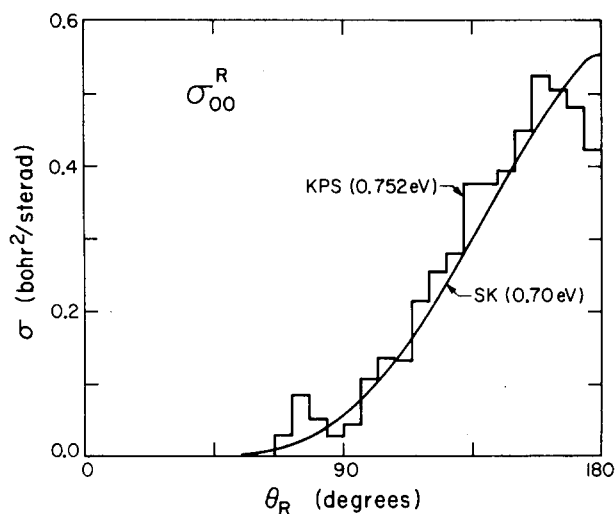


FIG. 26. Comparison of the differential reaction cross section  $\sigma_{00}^R$  as a function of the reactive scattering angle  $\theta_R$  as obtained by (a) the quasiclassical trajectory method of Karplus, Porter, and Sharma (the histogram labeled KPS) at  $E=0.752$  eV, and (b) the present coupled channel method (labeled SK) at 0.70 eV.

we have always computed scattering matrices for every partial wave required for convergence of the cross section. Another comparison of angular distributions is indicated in Fig. 28, where we examine the semiclassical

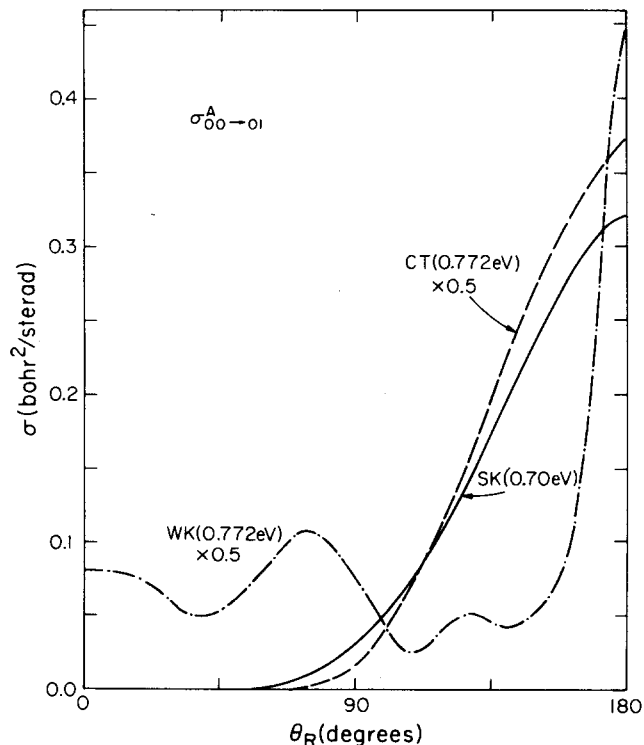


FIG. 27. Comparison of the differential cross section  $\sigma_{00}^{A-01}$  as a function of the reactive scattering angle  $\theta_R$  as calculated by (a) the distorted wave method of Choi and Tang (dashed curve labeled CT) at  $E=0.772$  eV, (b) the one vibration coupled-channel method of Wolken and Karplus (dash-dotted curve labeled WK) at  $E=0.772$  eV, and (c) the present method (solid curve labeled SK) at 0.70 eV.

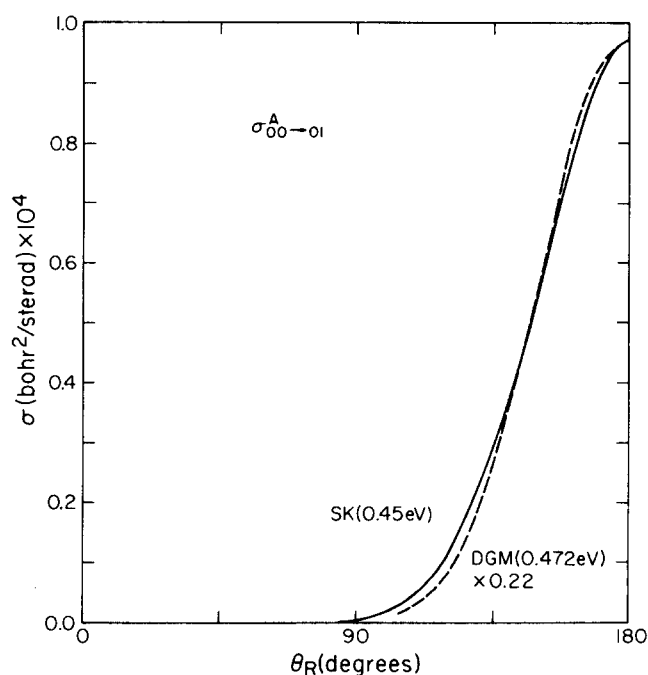


FIG. 28. Comparison of the semiclassical differential cross section  $\sigma_{00}^{A-01}$  as a function of the reactive scattering angle  $\theta_R$  calculated by Doll, George, and Miller (dashed curve labeled DGM) at 0.472 eV total energy with the corresponding  $\sigma_{00}^{A-01}$  of the present work (solid curve labeled SK) at 0.45 eV. The scaling factor of 0.22 was chosen so as to make the displayed curves coincide at  $\theta_R=180^\circ$ .

cal  $\sigma_{00}^{R-01}$  of Doll, George, and Miller<sup>8</sup> (DGM) at a much lower energy than has been considered in the previous two figures. The DGM cross sections are about 5 times larger than the present quantum ones, but the agreement between the shapes of the curves in Fig. 28 is excellent. In Fig. 29, the results of two methods (primitive semiclassical and classical semiclassical in the terminology of Ref. 53) used by DGM to calculate reaction probabilities are displayed. They are a factor 6–18 greater than the present ones. Presumably a “uniform” type of expression for evaluating the semiclassical reaction probability is required to bring those results into an agreement comparable to what was obtained in the same energy range for collinear  $H+H_2$ .<sup>53</sup> The results of Wolken and Karplus shown in the same figure are a factor of 10–30 greater than the present ones.

We conclude this section with a comparison of our nonreactive integral and differential cross sections with those of Wolken, Miller, and Karplus.<sup>22</sup> The latter calculation considered the same potential surface<sup>2c</sup> as did we but ignored the possibility of reactive collisions. A comparison of the resulting integral cross sections  $Q_{00-02}^N$  is given in Fig. 30. The two curves agree within the accuracy of the respective calculations, except perhaps at the highest energies considered. This is quite interesting, for WMK used a one-vibration-basis-function approximation (with, however,  $j_{max}=6$ ) in their calculation. This could indicate that the absence of closed vibrational channels is of much less significance for nonreactive collisions than it is for reactive ones.

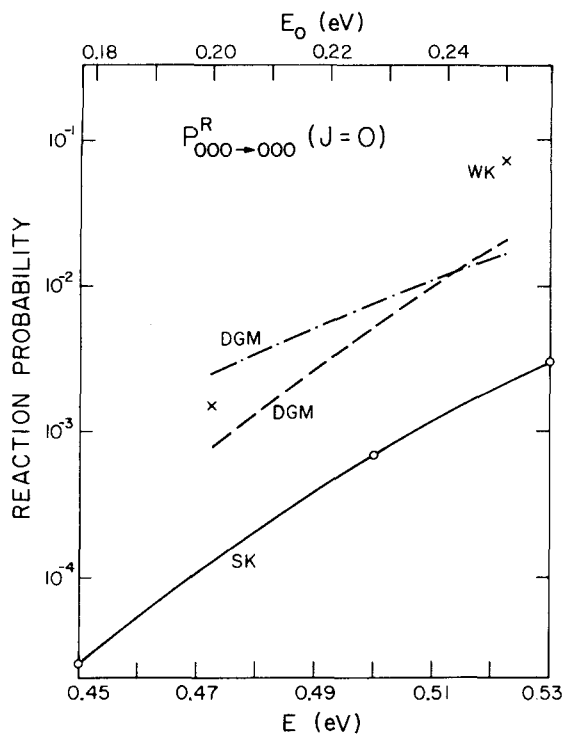


FIG. 29. Reaction probability  $P_{000 \rightarrow 000}^R$  for  $J=0$  as a function of the total energy  $E$  and translational energy  $E_0$ . The two curves labeled DGM are the semiclassical results of Doll, George, and Miller using the primitive semiclassical expression (dashed) and classical semiclassical expression (dash-dotted) in the terminology of Ref. 53. The two crosses are points from the work of Wolken and Karplus (WK), and the present results (SK) are denoted by circles and the solid line. The DGM and WK probabilities have been divided by 3 as described in Ref. 6 to make the comparison with our distinguishable-atom probabilities meaningful.

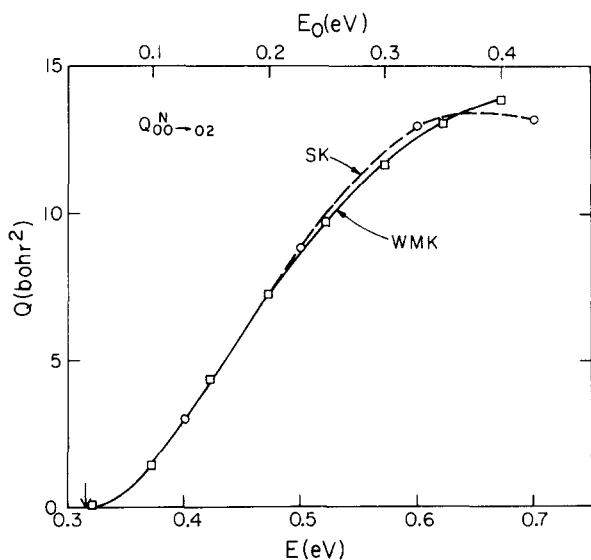


FIG. 30. Nonreactive integral cross section  $Q_{00 \rightarrow 02}^N$  as a function of the total energy  $E$  and translational energy  $E_0$ . The solid curve labeled WMK is the coupled-channel result of Wolken, Miller, and Karplus. (The actual points calculated are denoted by squares.) The present results (SK), given by circles, are connected by a dashed line. Arrow in abscissa indicates the energy at which the  $v=0$ ,  $j=2$  state of  $H_2$  becomes energetically accessible.

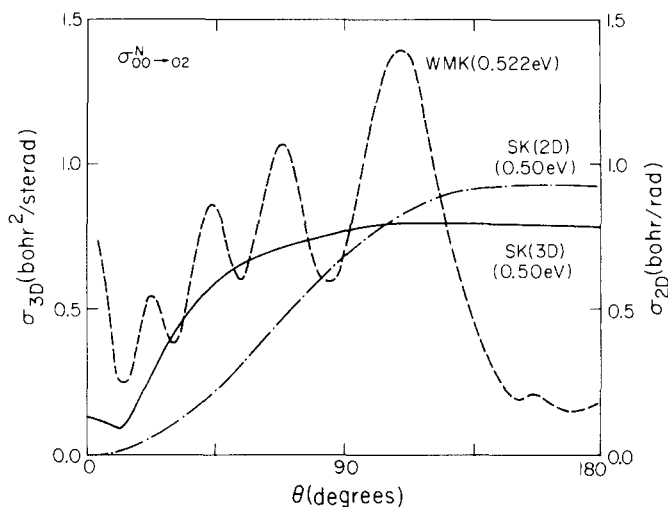


FIG. 31. Nonreactive differential cross section  $\sigma_{00 \rightarrow 02}^N$ . The dashed curve indicates the results of Wolken, Miller, and Karplus (WMK) at 0.522 eV. The present result (SK) at 0.50 eV is denoted by a solid curve, and the dash-dotted curve denotes the coplanar result (at 0.50 eV) of Ref. 13(b) with ordinate scale given on the right side of the graph.

Unfortunately, a comparison between the WMK differential cross sections  $\sigma_{00 \rightarrow 02}^N$  and ours (Fig. 31) shows a significant disagreement between them, with the WMK curve being highly oscillatory, in contrast with our very smooth one. We believe that the smooth behavior is more reasonable because (a) it is consistent with a direct mechanism being dominant in the collision process; (b) it agrees qualitatively with our coplanar result at the same energy (also plotted in Fig. 31) which is obtained from an entirely different calculation<sup>13b</sup>; and (c) it also qualitatively agrees with the corresponding nonreactive cross sections of Allison and Dalgarno<sup>23</sup> for the same system but a different interaction potential. Recently, Choi and Fang<sup>24b</sup> have used a coupled equations technique to recompute  $\sigma_{00 \rightarrow 02}^N$  for the same problem considered by WMK. They obtained a smooth angular distribution in very good agreement with our result. Note that Fig. 31 also shows the absence of any forward peak in the planar cross section. This is additional evidence for the conclusion of Sec. III B that the forward peak in the 3D result may be spurious.

#### H. Rate constants

In this section we will examine the behavior of the para-to-ortho rate constant for  $H+H_2$ . The ortho-to-para rate constant can be easily obtained from  $k_{p \rightarrow 0}(T)$  by using the readily available equilibrium constant.<sup>54</sup>

We first define the rate constant for the transition  $v_j m_j \rightarrow v' j' m_j'$  (valid for R, N, or A transitions):

$$k_{v_j m_j \rightarrow v' j' m_j'} = \langle Q_{v_j m_j \rightarrow v' j' m_j'} V_{v_j} \rangle$$

$$= \int Q_{v_j m_j \rightarrow v' j' m_j'}(V_{v_j}) V_{v_j} P(V_{v_j}) d^3 V_{v_j}, \quad (3.2)$$

where the velocities  $V_{v_j}$  were introduced in Sec. II A and  $P(V_{v_j})$  is the Boltzmann distribution function. Upon explicit substitution of this function into Eq. (3.2), we find

TABLE VII. Para-to-ortho thermal rate constants for H + H<sub>2</sub>.<sup>a</sup>

$T(K)$	$k_{p-o}(SK)$	$k_{p-o}^{dist}(SK)$	$k_{p-o}(KPS)^b$	$k_{p-o}(TST)^b$
100	0.270(4)	0.341(4)	0.783(-2)	0.405(-5)
200	0.688(7)	0.722(7)	0.375(6)	0.161(5)
250	0.753(8)	0.773(8)	0.127(8)	0.125(7)
300	0.442(9)	0.449(9)	0.136(9)	0.225(8)
400	0.486(10)	0.490(10)	0.268(10)	0.833(9)
500	0.224(11)	0.224(11)	0.168(11)	0.737(10)
600	0.640(11)	0.640(11)	0.595(11)	0.322(11)

<sup>a</sup>All rate constants are in units of cm<sup>3</sup>/(mole·sec). Quantum rate constants are believed accurate to 20%.

<sup>b</sup>Results of Ref. 3.

$$k_{vjm_j-v'j'm'_j} = N_A \left( \frac{8}{\pi\mu} \right)^{1/2} \frac{1}{(kT)^{3/2}} \times \int_0^\infty E_{vj}^{tr} Q_{vjm_j-v'j'm'_j}(E_{vj}^{tr}) e^{-E_{vj}^{tr}/kT} dE_{vj}^{tr}, \quad (3.3)$$

where  $\mu$  is the reduced mass corresponding to the motion of the atom with respect to the diatom and  $E_{vj}^{tr}$  is the translational energy relative to state  $vj(E_{vj}^{tr} = \frac{1}{2}\mu V_{vj}^2)$ .  $N_A$  is Avogadro's number, so that  $k$  has units of cm<sup>3</sup>/(mole·sec). Expressions for degeneracy-averaged rate constants  $k_{vj-v'j'}$  may be obtained by using the degeneracy averaged  $\sigma_{vj-v'j'}$  in Eq. (3.3) rather than  $\sigma_{vjm_j-v'j'm'_j}$ . The para-to-ortho rate constant is then obtained from the  $k_{vj-v'j'}$  via

$$k_{p-o}(T) = \sum_{(j \text{ even})} \frac{f_j(2j+1)e^{-E_{vj}/kT}}{Q_p(T)} \sum_{(j' \text{ odd})} k_{vj-v'j'}^A(T), \quad (3.4)$$

where

$$Q_p(T) = \sum_{(j \text{ even})} f_j(2j+1)e^{-E_{vj}/kT} \quad (3.5)$$

is the para-state reagent internal partition function and  $E_{vj}$  is the vibration rotation energy of state  $vj(E = E_{vj} + E_{vj}^{tr})$ . The nuclear spin degeneracy factor  $f_j$  has the value 1 for  $j$  even and 3 for  $j$  odd and thus is always unity for  $k_{p-o}$ . Calculation of this rate constant can be made using Eqs. (3.3)–(3.5) and the cross sections  $Q_{vj-ortho}^A$  which were defined at the end of Sec. II A. Some values of these integral cross sections are given in Table V. By evaluating the integral in the degeneracy-averaged counterpart of Eq. (3.3) numerically, we have obtained the para-to-ortho rate constants given in the second column of Table VII. Both linear and logarithmic interpolation were used between the energies at which cross sections were calculated and the results from the two methods agree to 20% or better. (The linear results are given in Table VII.) Only temperatures below 600 K have been used in the calculation because of substantial errors which occur in truncating the integral in Eq. (3.3) at 0.7 eV total energy for temperatures above 600 K.

The quantum para-to-ortho rate constant may also be obtained (approximately) from distinguishable atom cross sections. It is desirable to do this in order to provide additional comparisons between quantum and quasiclassical rate constants. The total reaction rate

constant  $k^R(T)$  for distinguishable atom collisions is<sup>3</sup>

$$k^R(T) = 2 \sum_{vj} \frac{f_j(2j+1)e^{-E_{vj}/kT}}{Q(T)} \sum_{v'j'} k_{vj-v'j'}^R(T), \quad (3.6)$$

where

$$Q(T) = \sum_{vj} f_j(2j+1)e^{-E_{vj}/kT}. \quad (3.7)$$

The factor of 2 at the beginning of the right-hand side of Eq. (3.6) arises from an explicitly performed sum over the two equivalent product arrangement channels. In the limit in which a large number of quantum states contribute to the sums in Eqs. (3.4) and (3.6), we may assume that a sum of rate constants over just odd product states (or just even states) is approximately half the sum over all possible states, i.e.,

$$\sum_{\substack{v'j' \\ (j' \text{ odd}) \\ (j' \text{ even})}} k_{vj-v'j'}^R(T) \sim \frac{1}{2} \sum_{(all j')} k_{vj-v'j'}^R(T). \quad (3.8)$$

In addition, for high enough temperatures,

$$Q_0 = \sum_{(j \text{ odd})} f_j(2j+1)e^{-E_{vj}/kT} \sim 3 \sum_{(j \text{ even})} f_j(2j+1)e^{-E_{vj}/kT} = 3Q_p, \quad (3.9)$$

so that

$$Q = Q_0 + Q_p \sim 4Q_p. \quad (3.10)$$

By realizing that  $k_{o-p}$  is given by an expression analogous to Eqs. (3.4) and (3.5) but with the even and odd sums interchanged, and by combining the expressions for  $k_{o-p}$  and  $k_{p-o}$ , using Eqs. (3.8)–(3.10) and the relations between antisymmetrized and distinguishable reactive rate constants implicit in the discussion following Eq. (2.8), we find

$$k^R(T) \sim k_{p-o}(T) + k_{o-p}(T) \sim k_{p-o}(T) \left( 1 + \frac{1}{K_{eq}} \right), \quad (3.11)$$

where  $K_{eq}$  is the equilibrium constant. To the same order of approximation, Eq. (3.9) implies that  $K_{eq} \sim 3$ , so Eq. (3.11) yields

$$k^R(T) \sim \frac{4}{3} k_{p-o}(T). \quad (3.12)$$

This implies that by computing  $k^R(T)$  and using Eqs. (2.12) and (3.11) or (3.12), we can approximately compute  $k_{p-o}(T)$  from distinguishable-atom reactive cross sections  $Q^R$ . In the third column of Table VII we list the  $k_{p-o}^{dist}$  so obtained. Equation (3.11) (in which  $K_{eq}$  is not assumed to have the value 3) was found to give slightly better agreement between  $k_{p-o}^{dist}$  and  $k_{p-o}$  for  $T < 300$  K than Eq. (3.12) and was therefore used in calculating  $k_{p-o}^{dist}$  in the table. We see that for  $T \geq 300$  K,  $k_{p-o}^{dist}(T)$  and  $k_{p-o}(T)$  are identical to at least two significant features indicating that the approximation is quite accurate even at fairly low temperatures. If we use Eq. (3.11) to convert the Karplus, Porter, and Sharma<sup>3</sup> rate constant  $k^R(KPS)$  to  $k_{p-o}(KPS)$ , we obtain the results in the fourth column of Table VII. In the fifth column we have listed the analogous transition state theory result  $k_{p-o}(TST)$  without tunneling corrections [which is obtained from Eq. (3.11) and the formula given in Ref. 3]. Note that transition state theory

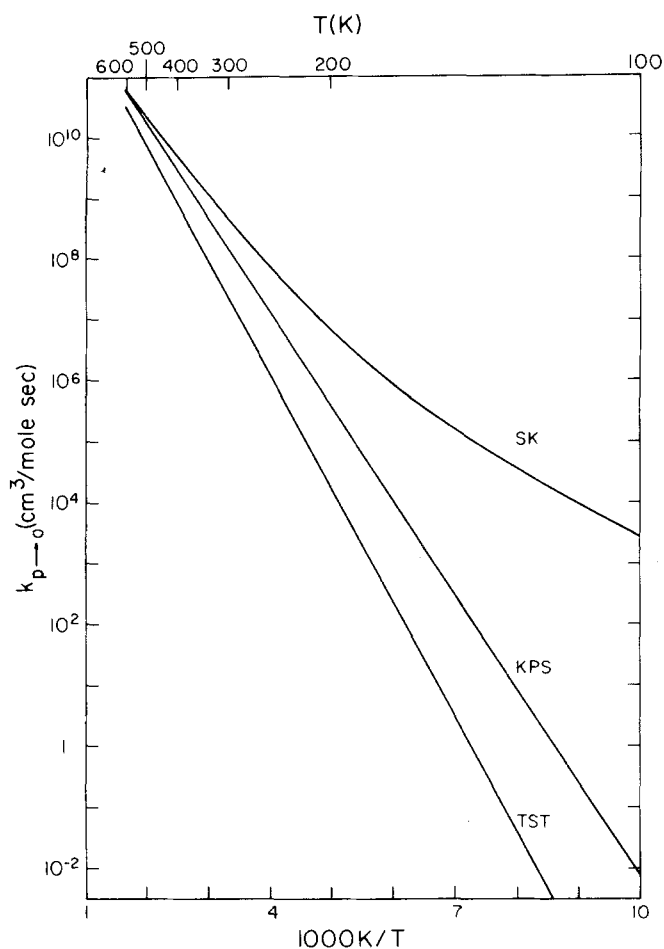


FIG. 32. Arrhenius plot of the para-to-ortho thermal rate constant. The present quantum result is denoted by SK, while the quasiclassical result of Karplus, Porter, and Sharma is labeled KPS and the transition state theory result is labeled TST.

ordinarily does not distinguish different possible product spin states, so that in order to define  $k_{p \rightarrow o}(\text{TST})$ , we have to make the additional obvious assumption that the individual nuclear spins are good constants of the motion. It is worthwhile noting here that a number of rate constants in addition to those in Table VII may be calculated, but most of these additional rate constants provide no new information (see also Ref. 55). For example, any ortho-to-para rate constant is simply  $k_{o \rightarrow p} = k_{p \rightarrow o}/K_{op}$ , and any distinguishable-atom rate constant  $k_{p \rightarrow o}^{\text{dist}}$  (which includes those in the last three columns of Table VII) may be related to the corresponding total rate constant using Eq. (3.11). One exception is the quasiclassical para-to-ortho rate constant  $k_{p \rightarrow o}^R$  which is obtained by selecting only those trajectories which fall into bins connecting even and odd states. This quantity cannot be extracted from the results of Ref. 3, and is only approximated by  $k_{p \rightarrow o}(\text{KPS})$  as obtained using Eq. (3.11).

Arrhenius plots of the quantum, quasiclassical, and transition state theory rate constants are presented in Fig. 32. At 600 K, the quasiclassical  $k_{p \rightarrow o}(\text{KPS})$  differs from  $k_{p \rightarrow o}(\text{SK})$  by only 7%, while the TST result is in error by 79%. The close agreement of the quasiclassi-

cal and quantum results is an obvious consequence of the excellent agreement of the corresponding integral cross sections (above the classical thresholds) in Fig. 24 coupled with the excellent validity of Eqs. (3.11) and (3.12). Presumably, the quantum and quasiclassical rate constants will continue to be in very good agreement at temperatures above 600 K. At lower temperatures, however, tunneling effects become extremely important with  $k_{p \rightarrow o}(\text{SK})$  a factor of 3.3 larger than  $k_{p \rightarrow o}(\text{KPS})$  at 300 K and 18 times larger at 200 K. The significant nonlinearity in the quantum curve in Fig. 31 is also apparently related to tunneling, although we should note that previous studies on collinear  $\text{H} + \text{H}_2$  have shown<sup>56</sup> that tunneling can make significant contributions to the rate constant even at 1000 K where the collinear reaction Arrhenius plot is quite linear. The transition state theory rate constant deviates from  $k_{p \rightarrow o}(\text{SK})$  even more severely than  $k_{p \rightarrow o}(\text{KPS})$ , with  $k_{p \rightarrow o}(\text{SK})/k_{p \rightarrow o}(\text{TST})$  being 20 at 300 K and 427 at 200 K. Part of the error in the TST result is probably due to the neglect of tunneling corrections in the expression used<sup>3</sup> (i. e., a transmission coefficient of unity has been assumed). For a scaled version<sup>14a</sup> of the SSMK surface,<sup>2d</sup> Truhlar and Kuppermann<sup>14a</sup> have calculated vibrationally adiabatic zero curvature (VAZC) transmission coefficients of 0.903 at 600 K, 0.98 at 300 K, and 1.72 at 200 K, thus indicating that inclusion of these factors is not apt to improve the situation significantly. In addition, the ratio  $k_{p \rightarrow o}(\text{KPS})/k_{p \rightarrow o}(\text{TST})$  deviates substantially from unity in Table VII despite the fact that tunneling has been omitted from both calculations. Because of the strongly nonlinear behavior of  $k_{p \rightarrow o}(\text{SK})$  in Fig. 32, the attempt to characterize that rate constant by a single activation energy is probably not too meaningful. If one does, however, compute such a quantity by arbitrarily fitting a straight line between the 500 K and 600 K points, one finds activation energies of 6.3, 7.5, and 8.8 kcal/mole for  $k_{p \rightarrow o}(\text{SK})$ ,  $k_{p \rightarrow o}(\text{KPS})$ , and  $k_{p \rightarrow o}(\text{TST})$ , respectively. The quantum activation energy is 1.1 kcal/mole (0.048 eV) above the corresponding coplanar one (5.2 kcal/mole),<sup>13b</sup> and this difference is almost identical to the 0.05 eV 2D to 3D shift observed in Figs. 19 and 20 for the reaction probability curves.

Since the Porter-Karplus potential surface we used has an incorrect barrier height (0.396 eV<sup>2c</sup> vs 0.425 eV for the more accurate Liu surface<sup>1e</sup>), a comparison with experimental results of thermal rate constant measurements will be deferred to a paper in which the results obtained with the full noncollinear Liu surface are described.

#### IV. SUMMARY

Let us now summarize the significant concepts developed in this paper. First, in the analysis of the reactive transition probabilities and cross sections we found a fairly accurate rotational projection quantum number (i. e., polarization) selection rule ( $m_j = m'_j = 0$ ). Although one can find many factors which are at least partially responsible for this effect, the primary reason for this specificity and selectivity is the restriction to nearly linear geometries in the transition state as is

determined by the potential energy surface. No comparable selection effect was found for the nonreactive collisions (compare, for example, Figs. 10 and 11). At higher energies, quantum symmetry interference oscillations were observed in the  $j = 0$  to  $j' = 2$  para-to-para differential cross sections (see Fig. 15). Such oscillations might be capable of interpretation in terms of parameters which characterize the potential energy surface as has been done for the related atom-diatom and molecule-molecule elastic scattering situations.<sup>57</sup> The elastic cross sections revealed a lack of sensitivity of the  $\theta < 30^\circ$  angular distributions to the loss of flux into inelastic and reactive channels, and demonstrated the approximate validity of Levine's<sup>45</sup> conservation of total cross section rule and the validity of the central field approximation in this angular range. A comparison of the results of 1D, 2D, and 3D calculations revealed the importance of bending motions in the transition state and demonstrated their connection with threshold energies. In addition, the orientation dependence of the reaction probabilities was analyzed and found to be compatible with the observed maximum values of the total reaction probabilities. The results of 1D, 2D, and 3D comparisons afforded in this paper should be of great use in the improvement of 1D and 2D models so that they can be used to make quantitative predictions about 3D results. The degeneracy-averaged rotational distributions were found to obey Boltzmann-like expressions with a surprising degree of accuracy. A precise understanding of why this occurs remains unknown at present, but an analysis of the scattering wavefunction at the transition state in terms of vibrationally and rotationally adiabatic wavefunctions may help to clarify the relation of bending energy to product state rotational energy and hence to the temperature parameter. A comparison of our integral and differential cross sections with those of several other approximate calculations indicates best agreement with the quasiclassical results at energies for which tunneling effects are not important. On the other hand, the lack of tunneling in the classical cross sections produces important differences in the para-to-ortho thermal rate constant at temperatures below 300 K but the agreement is good at 600 K.

The wealth of dynamical information presented here makes clear the great usefulness of these calculations. At the same time, the large expenditure of computer time indicated in Table II implies that analogous calculations will be done for only a limited number of additional systems for which a very detailed understanding of the important dynamical processes involved is highly desirable. This places prime emphasis on the development of accurate but efficient approximate techniques, and the comparisons between accurate results and approximate ones such as those considered in Secs. III E and III G and in decoupling schemes presently being used by us indicate that such techniques may indeed exist.

#### ACKNOWLEDGMENT

We thank Ambassador College for generous use of their computational facilities. We also thank

Professor Donald G. Truhlar for useful comments.

\*Research supported in part by the United States Air Force Office of Scientific Research (Grant No. AFOSR-73-2539).

<sup>†</sup>Work performed in partial fulfillment of the requirements for the Ph. D. in Chemistry at the California Institute of Technology. Present address: Department of Chemistry, Northwestern University, Evanston, Illinois 60201.

<sup>‡</sup>Contribution No. 5251.

<sup>1</sup>(a) P. A. M. Dirac, Proc. R. Soc. London Ser. A 123, 714 (1929); (b) E. Schrödinger, Ann. Phys. 79, 361, 489 (1925); 80, 437 (1926); 81, 109 (1926).

<sup>2</sup>(a) F. London, Z. Elektrochem. 35, 552 (1929); H. Eyring and M. Polanyi, Z. Phys. Chem. B 12, 279 (1931); (b) S. Sato, J. Chem. Phys. 23, 592 (1955); (c) R. N. Porter and M. Karplus, J. Chem. Phys. 40, 1105 (1964); (d) I. Shavitt, R. M. Stevens, F. L. Minn, and M. Karplus, J. Chem. Phys. 48, 2700 (1968); (e) H. Conroy and B. Bruner, J. Chem. Phys. 42, 4047 (1965); *ibid.* 47, 921 (1967); (f) B. Liu, J. Chem. Phys. 58, 1925 (1973); (g) see also C. Edmiston and M. Krauss, J. Chem. Phys. 49, 192 (1968) and references therein.

<sup>3</sup>M. Karplus, R. N. Porter, and R. D. Sharma, J. Chem. Phys. 43, 3259 (1965).

<sup>4</sup>D. Micha, Ark. Fys. 30, 427 (1965).

<sup>5</sup>M. Karplus and K. T. Tang, Discuss. Faraday Soc. 44, 56 (1967); K. T. Tang and M. Karplus, Phys. Rev. A. 4, 1844 (1971).

<sup>6</sup>J. D. Doll, T. F. George, and W. H. Miller, J. Chem. Phys. 58, 1343 (1973).

<sup>7</sup>G. Wolken and M. Karplus, J. Chem. Phys. 60, 351 (1974).

<sup>8</sup>(a) B. H. Choi and K. T. Tang, J. Chem. Phys. 61, 2462 (1974); (b) *ibid.* 61, 5147 (1974).

<sup>9</sup>A. Kuppermann and G. C. Schatz, J. Chem. Phys. 62, 2502 (1975).

<sup>10</sup>A. B. Elkowitz and R. E. Wyatt, J. Chem. Phys. 62, 2504 (1975).

<sup>11</sup>(a) R. P. Saxon and J. C. Light, J. Chem. Phys. 56, 3874 (1972); *ibid.* 56, 3885 (1972); (b) A. Altenberger-Siczek and J. C. Light, J. Chem. Phys. 61, 4373 (1974); (c) R. P. Saxon and J. C. Light, J. Chem. Phys. 57, 2758 (1972); (d) J. J. Tyson, R. P. Saxon, and J. C. Light, J. Chem. Phys. 59, 363 (1973).

<sup>12</sup>R. B. Walker and R. E. Wyatt, J. Chem. Phys. 61, 4839 (1974).

<sup>13</sup>(a) A. Kuppermann, G. C. Schatz, and M. Baer, J. Chem. Phys. 61, 4362 (1974); (b) G. C. Schatz and A. Kuppermann, J. Chem. Phys. 65, 4624 (1976), two papers back.

<sup>14</sup>(a) D. G. Truhlar and A. Kuppermann, J. Chem. Phys. 56, 2232 (1972); (b) *ibid.*, references therein.

<sup>15</sup>(a) H. Eyring, J. Chem. Phys. 3, 107 (1935); H. Pelzer and E. Wigner, Z. Phys. Chem. B 15, 445 (1932); (b) H. S. Johnston, *Gas Phase Reaction Rate Theory* (Ronald, New York, 1966), Chap. 10.

<sup>16</sup>I. Shavitt, J. Chem. Phys. 49, 4048 (1969).

<sup>17</sup>J. M. Bowman, A. Kuppermann, J. T. Adams, and D. G. Truhlar, Chem. Phys. Lett. 20, 229 (1973); J. M. Bowman, Ph. D. thesis, California Institute of Technology, 1974.

<sup>18</sup>D. J. Diestler, J. Chem. Phys. 56, 2092 (1972).

<sup>19</sup>(a) R. D. Levine and S. F. Wu, Chem. Phys. Lett. 11, 557 (1971); S. F. Wu and R. D. Levine, Mol. Phys. 22, 881 (1971).

<sup>20</sup>G. C. Schatz and A. Kuppermann, J. Chem. Phys. 59, 964 (1973).

<sup>21</sup>G. C. Schatz and A. Kuppermann, Phys. Rev. Lett. 35, 1266 (1975).

<sup>22</sup>G. Wolken, W. H. Miller, and M. Karplus, J. Chem. Phys. 56, 4930 (1972).

<sup>23</sup>A. C. Allison and A. Dalgarno, Proc. Phys. Soc. London 90, 609 (1967).

- <sup>24</sup>(a) K. T. Tang, Phys. Rev. 187, 122 (1969); (b) B. H. Choi and K. T. Tang, J. Chem. Phys. 63, 1783 (1975).
- <sup>25</sup>E. F. Hayes, C. A. Wells, and D. J. Kouri, Phys. Rev. A 4, 1017 (1971).
- <sup>26</sup>A. A. Westenberg and N. de Haas, J. Chem. Phys. 47, 1393 (1967); D. N. Mitchell and D. J. LeRoy, J. Chem. Phys. 58, 3449 (1973); see Ref. 15(b) for earlier references.
- <sup>27</sup>A. Kuppermann and J. M. White, J. Chem. Phys. 44, 4352 (1966); A. Kuppermann, in *Proceedings of the Nobel Symposium 5 on Fast Reactions in Primary Processes in Chemical Kinetics*, edited by S. Claesson (Interscience, New York, 1967), pp. 131–140; Israel J. Chem. 7, 303 (1969).
- <sup>28</sup>J. Geddes, H. F. Krause, and W. L. Fite, J. Chem. Phys. 52, 3296 (1970); *ibid.* 56, 3298 (1972); *ibid.* 59, 566 (1973); G. H. Kwei, V. W. S. Lo, and E. A. Entemann, J. Chem. Phys. 59, 3421 (1973); S. Datz and E. H. Taylor, J. Chem. Phys. 39, 1896 (1963).
- <sup>29</sup>G. C. Schatz and A. Kuppermann, J. Chem. Phys. 65, 4642 (1976), preceding paper.
- <sup>30</sup>A. Kuppermann, G. C. Schatz and M. Baer, J. Chem. Phys. 65, 4596 (1976), three papers back.
- <sup>31</sup>A. Kuppermann, Chem. Phys. Lett. 32, 374 (1975).
- <sup>32</sup>A. S. Davydov, *Quantum Mechanics* (Addison-Wesley, Reading, MA, 1965), Chap. 6.
- <sup>33</sup>Equation (2.7) can be proven by considering the effect of the inversion operator  $\theta$  of Appendix B of Ref. 29 on the scattering matrix solution  $\Psi_{JM}^{\lambda'v'j'\lambda'\Omega\lambda}[S]$  of Eq. (5.3) of Ref. 29. By using Eqs. (B4) and (5.5) of that paper, one can easily show that the incident spherical wave parts of  $(-1)^J \Psi_{JM}^{\lambda'v'j'\lambda'\Omega\lambda}$  and  $\Psi_{JM}^{\lambda'v'j'\lambda'\Omega\lambda}$  are identical and as a result so are the corresponding outgoing parts, from which we conclude that  $S_{J\lambda'v'j'\lambda'\Omega\lambda}^{\lambda'v'j'\lambda'\Omega\lambda}$  and  $S_{J\lambda'v'j'\lambda'\Omega\lambda}^{\lambda'v'j'\lambda'\Omega\lambda}$  are equal. According to Eq. (5.30) of Ref. 29, we may replace  $-\Omega_\lambda'$  by  $m_\lambda'$ , whereas  $\Omega_\lambda$  may be replaced by  $m_\lambda$ . From this results  $S_{J\lambda'v'j'\lambda'\Omega\lambda}^{\lambda'v'j'\lambda'\Omega\lambda} = S_{J\lambda'v'j'\lambda'\Omega\lambda}^{\lambda'v'j'\lambda'\Omega\lambda}$ , which when substituted into Eq. (2.2) (of the present paper) together with the property<sup>32</sup>
- $$d_{m_\lambda' m_\lambda}^J(\theta) = (-1)^{m_\lambda' - m_\lambda} d_{-m_\lambda' -m_\lambda}^J(\theta)$$
- yields the relation
- $$\frac{\lambda' v_\lambda' j_\lambda' - m_\lambda'}{f \lambda_\lambda' j_\lambda - m_\lambda} = (-1)^{m_\lambda' - m_\lambda} \frac{\lambda' v_\lambda' j_\lambda' m_\lambda}{f \lambda_\lambda' j_\lambda m_\lambda}$$
- from which Eq. (2.7) follows.
- <sup>34</sup>The various expansion coefficients  $V_k^\lambda$  of Eq. (2.14) were evaluated using a procedure outlined in Ref. 13(b) in which the  $n$ -term truncated expansion in Eq. (2.14) is required to be exactly satisfied at  $n$  values of  $\gamma_\lambda$  and the  $V_k^\lambda$  are obtained algebraically from this condition.
- <sup>35</sup>This number can be obtained from a time delay analysis of the scattering matrix, similar to the one described previously.<sup>20</sup>
- <sup>36</sup>R. G. Newton, *Scattering Theory of Waves and Particles* (McGraw-Hill, New York, 1966), pp. 572–575.
- <sup>37</sup>R. T. Pack, J. Chem. Phys. 60, 633 (1974); P. McGuire and D. J. Kouri, J. Chem. Phys. 60, 2488 (1974).
- <sup>38</sup>This can be verified by examining the expressions for  $J_z$  and  $H$  given in Ref. 29.
- <sup>39</sup>This follows from (a) the assumption of Ref. 29 [which is implicit in Eq. (2.3)] that the initial relative velocity vector is parallel to the space fixed  $z$  axis, (b) the definition of the angle  $\theta$  (or  $\theta_\lambda$  of Fig. 1), which is the angle between the outgoing  $z_\lambda'$  axis and the space-fixed  $z$  axis, and (c) the relation  $\theta_R = 180 - \theta$  of Sec. II A.
- <sup>40</sup>For example, R. Gengenback, C. Hahn, and J. P. Toennies, J. Chem. Phys. 62, 3620 (1975); M. A. Fluendy, R. M. Martin, E. E. Muschlitz, and D. R. Herschbach, J. Chem. Phys. 46, 2172 (1967); W. C. Stwalley, A. Niehaus, and D. R. Herschbach, J. Chem. Phys. 51, 2287 (1969).
- <sup>41</sup>A. Kuppermann, R. J. Gordon, and M. J. Coggiola, J. Chem. Soc. Faraday Discuss. 55, 145 (1973).
- <sup>42</sup>H. P. Butz, R. Feltgen, H. Pauly, and H. v. Vehmeyer, Z. Phys. 247, 70 (1971).
- <sup>43</sup>R. Gordon, J. Chem. Phys. 51, 14 (1969).
- <sup>44</sup>Some ambiguity still exists because of the small difference ( $< 0.05$  rad) between the single channel and converged phase shifts.
- <sup>45</sup>R. D. Levine, Chem. Phys. Lett. 4, 309 (1969); J. Chem. Phys. 57, 1015 (1972).
- <sup>46</sup>(a) D. J. Diestler, J. Chem. Phys. 54, 4547 (1971); (b) J. W. Duff and D. G. Truhlar, Chem. Phys. Lett. 23, 327 (1973).
- <sup>47</sup>R. B. Walker and R. E. Wyatt, Mol. Phys. 28, 101 (1974).
- <sup>48</sup>A. Ben-Shaul, R. D. Levine, and R. B. Bernstein, Chem. Phys. Lett. 15, 160 (1972); J. Chem. Phys. 57, 5427 (1972).
- <sup>49</sup>R. E. Wyatt, Chem. Phys. Lett. 34, 167 (1975).
- <sup>50</sup>A. C. Yates and W. A. Lester, Chem. Phys. Lett. 24, 305 (1974).
- <sup>51</sup>R. E. Wyatt (private communication).
- <sup>52</sup>A. B. Elkowitz and R. E. Wyatt, J. Chem. Phys. 63, 702 (1975).
- <sup>53</sup>J. M. Bowman and A. Kuppermann, J. Chem. Phys. 59, 6524 (1973); W. H. Miller and T. F. George, J. Chem. Phys. 57, 2458 (1972).
- <sup>54</sup>A. Farkas, *Orthohydrogen, Parahydrogen and Heavy Hydrogen* (Cambridge U. P., Cambridge, 1935), p. 13.
- <sup>55</sup>D. G. Truhlar, J. Chem. Phys. 65, 1008 (1976).
- <sup>56</sup>A. Kuppermann, J. T. Adams, and D. G. Truhlar, (to be published).
- <sup>57</sup>For examples, see J. M. Farrar and J. T. Lee, J. Chem. Phys. 56, 5801 (1972); P. E. Siska, J. M. Parson, T. P. Schaefer, and Y. T. Lee, J. Chem. Phys. 55, 5762 (1971); J. M. Farrar and Y. T. Lee, J. Chem. Phys. 57, 5492 (1972).